ACS OMEGA

http://pubs.acs.org/journal/acsodf

Article

Deep Insights into the Coupled Optoelectronic and Photovoltaic Analysis of Lead-Free $CsSnI_3$ Perovskite-Based Solar Cell Using DFT Calculations and SCAPS-1D Simulations

M. Khalid Hossain,* G. F. Ishraque Toki, D. P. Samajdar,* Muhammad Mushtaq, M. H. K. Rubel,* Rahul Pandey,* Jaya Madan, Mustafa K. A. Mohammed, Md. Rasidul Islam, Md. Ferdous Rahman, and H. Bencherif

Cite This: *ACS Omega* 2023, 8, 22466−22485

Read Online

ACCESS | Metrics & More | Article Recommendations

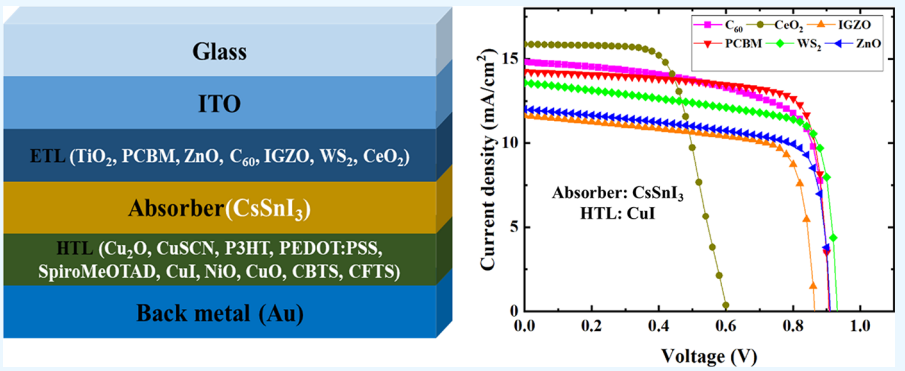

ABSTRACT: $CsSnI_3$ is considered to be a viable alternative to lead (Pb)-based perovskite solar cells (PSCs) due to its suitable optoelectronic properties. The photovoltaic (PV) potential of $CsSnI_3$ has not yet been fully explored due to its inherent difficulties in realizing defect-free device construction owing to the nonoptimized alignment of the electron transport layer (ETL), hole transport layer (HTL), efficient device architecture, and stability issues. In this work, initially, the structural, optical, and electronic properties of the $CsSnI_3$ perovskite absorber layer were evaluated using the CASTEP program within the framework of the density functional theory (DFT) approach. The band structure analysis revealed that $CsSnI_3$ is a direct band gap semiconductor with a band gap of 0.95 eV, whose band edges are dominated by Sn 5s/5p electrons After performing the DFT analysis, we investigated the PV performance of a variety of $CsSnI_3$-based solar cell configurations utilizing a one-dimensional solar cell capacitance simulator (SCAPS-1D) with different competent ETLs such as IGZO, WS_2, CeO_2, TiO_2, ZnO, PCBM, and C_{60}. Simulation results revealed that the device architecture comprising ITO/ETL/$CsSnI_3$/CuI/Au exhibited better photoconversion efficiency among more than 70 different configurations. The effect of the variation in the absorber, ETL, and HTL thickness on PV performance was analyzed for the above-mentioned configuration thoroughly. Additionally, the impact of series and shunt resistance, operating temperature, capacitance, Mott−Schottky, generation, and recombination rate on the six superior configurations were evaluated. The $J-V$ characteristics and the quantum efficiency plots for these devices are systematically investigated for in-depth analysis. Consequently, this extensive simulation with validation results established the true potential of $CsSnI_3$ absorber with suitable ETLs including ZnO, IGZO, WS_2, PCBM, CeO_2, and C_{60} ETLs and CuI as HTL, paving a constructive research path for the photovoltaic industry to fabricate cost-effective, high-efficiency, and nontoxic $CsSnI_3$ PSCs.

1. INTRODUCTION

To keep pace with the current growth of solar technologies, perovskite solar cells (PSCs) have garnered significant research owing to the significant rise in efficiency from a meager 3.8 to 25.7% within a decade.[1−5] This significant improvement has been made possible due to the excellent optoelectronic characteristics of halide perovskite materials used including their high absorption coefficient, low exciton binding energies, long-range charge diffusion lengths, acceptable band gaps, and

Received: January 15, 2023
Accepted: May 10, 2023
Published: June 14, 2023

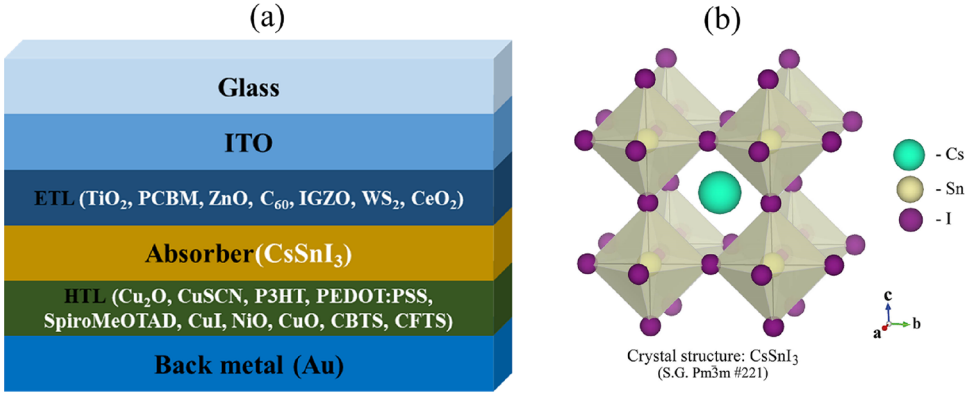

Figure 1. (a) Design configuration of the $CsSnI_3$-based PSC, and (b) the optimized crystal structure of $CsSnI_3$ perovskite.

high charge carrier mobilities.[2,3,5−8] As light absorbers in PSCs, hybrid organic−inorganic halide perovskites, particularly methylammonium lead triiodide ($MAPbI_3$) and formamidinium lead triiodide ($FAPbI_3$) have received the majority of attention at this point. The major hindrance toward the path of commercialization and efficient usage of $MAPbI_3$ or $FAPbI_3$-based PSCs is due to the constituent element lead (Pb), which is highly toxic in nature.[9,10] Under these circumstances, the European Union and other nations have placed strong restrictions on the usage of Pb-containing materials in electronic gadgets, which has accelerated the research on Pb-free PSCs.[3,11] Due to the low toxicity and exceptional theoretical PCE, lead-free tin halide perovskites have received a lot of attention in the development of energy-efficient SCs.[12] Tin (Sn) is considered one of the most practical substitutes for Pb in the perovskite configurations as replacement of the toxic Pb^{2+} ions with Sn^{2+} creates no alteration in the perovskite structure owing to the similarity between the outer shell of Pb and Sn.[13] Hence, $MASnI_3$ and $FASnI_3$ have been thoroughly investigated for PV applications and it is predicted that the conversion of the organic−inorganic hybrid perovskite to all-organic perovskite through the replacement of MA^+ or FA^+ with Cesium (Cs) leads to the enhancement in the intrinsic phase and thermal stability.[14−17]

It has been demonstrated in the literature that the all-inorganic $CsSnI_3$ perovskite can be produced via melting−solidification and has a melting point of 451 °C, signifying superior inherent thermal stability.[18,19] In contrast, the $MASnI_3$ and $FASnI_3$ perovskite analogs of halide perovskites begin to deteriorate at about ∼200 °C.[20] The aforementioned factors contribute to the motivation for the exploration of $CsSnI_3$ material as a potentially useful thermally durable, lead-free perovskite for next-generation PSCs. For device-operating temperatures in the range 20−100 °C, $CsSnI_3$ exists in the form of two polymorphs: the desired "black" B−γ−$CsSnI_3$ stage and the unfavorable "yellow" Y—$CsSnI_3$ stage.[18] Comprehensive research has been done on the B−γ−$CsSnI_3$ stage, and it has been found to have features that are useful for PSC applications. It has a direct ideal band gap of 1.3 eV,[18,21] a low exciton binding energy of 10−20 meV,[22] a significant optical absorption coefficient of $\sim 10^4$ cm^{-1},[23] and high hole mobility of up to ∼585 cm^2 V^{-1} s^{-1}.[18] However, there are just a few findings that have employed B−γ−$CsSnI_3$ as a light absorber in modules, and those findings have had varying degrees of success, underlining the difficulties in developing B−γ−$CsSnI_3$-based PSCs.[24,25]

A thorough grasp of how the different constituent layers, namely, the transparent conductive oxide (TCO), perovskite absorber layer (PAL), hole transport layer (HTL), the electron transport layer (ETL), and back-metal contact layers in PSCs, affecting solar cell (SC) performance, is crucial for optimizing and enhancing PSC performance.[26−28] The optical absorption characteristics of the PAL play a dominant role in influencing the PV characteristics. The transportation and extraction of the charge carriers produced due to the absorption of photons in the PAL are controlled by the ETL and HTL.[29] While the open circuit voltage (V_{OC}) is determined by the Fermi energy level difference among the ETL and HTL; the ETL's accelerated charge mobility causes a commensurate rise in the fill factor (FF) and short circuit current density (J_{SC}).[30−32] Materials utilized as ETL and HTL include both organic and inorganic components. The most commonly used ETLs like TiO_2,[33,34] ZnO,[33,35] C_{60},[36] IGZO,[37] PCBM, WS_2,[34,38] and CeO_2[39] are used with CuI[40] and CBTS[41] is as HTL, due to the suitable respective band gap, charge mobility, band alignment, and transparency.

In order to predict the suitability of a particular material system for PV applications, we need to investigate its optical and electronic properties systematically and accurately and this necessitates the usage of DFT approaches,[42] which have gained a lot of popularity in physical, chemical, and biological applications since its inception in the 1970s.[43] Song et al. computed the structural and electronic properties of $CsSnI_3$ based on the DFT approach using PBEsol exchange-correlation functional implemented in the VASP package to conclude that the polar phase ($Pmc2_1$) possesses a direct tunable band gap in the range 0.42−1.41 eV, which is suitable for light-harvesting applications.[44] The electronic band structure of $CsSnI_3$ computed using the quasiparticle self-consistent GW method revealed a band gap of 1.3 ± 0.1 eV for $CsSnI_3$, high hole mobility, and a low exciton binding energy of 0.1 meV.[45] First-principle calculations reveal that the band gap of $CsSnI_3$ varies from ∼1.2−1.3 eV over a temperature range from 9 to 300 K due to the change in the lattice constant with a linear thermal expansion coefficient of 1.40×10^5 K^{-1}.[46] Traoré et al. reported a band gap of 1.21 eV for $CsSnI_3$ using the reoptimized Tran−Blaha-modified Becke−Johnson (TB-mBJ) potential, which is much higher than the underestimated band gap of nearly zero computed using local density approximation.[47] In order to check the feasibility of using $CsSnI_3$ as a potential absorber for SCs, we have systematically investigated the structural, optical, and electronic properties of the perovskite along with its charge density characteristics and Fermi surface topology within the framework of DFT calculations using the CASTEP software. The best-optimized ground state was utilized for the evaluation of the above-mentioned properties of the $CsSnI_3$ absorber.

https://doi.org/10.1021/acsomega.3c00306
ACS Omega 2023, 8, 22466−22485

The functionality of the device can be improved by combining the perovskite absorber layer with acceptable replacements for conventional ETL, HTL, and back contact metals. By selecting 70 different configurations in the Solar Cell Capacitance Simulator-1D (SCAPS-1D), we thoroughly evaluated the suitability of a variety of ETLs and HTLs in this work to find the ideal combination for the $CsSnI_3$ absorber layer for achieving superior PV performance in comparison to the existing works. We performed a computational study to create a combination of heterostructures to reduce the time and cost complexity needed to fabricate such a vast number of SC configurations physically. Based on these considerations, 70 various combinations of ITO/ETL/$CsSnI_3$/HTL/Au heterostructures have been examined for the $CsSnI_3$-based PV configurations with a broad variety of HTLs including Cu_2O, CuSCN, NiO, P3HT, CBTS, PEDOT:PSS, Spiro-MeOTAD, CuI, CuO, and CFTS combined with ETLs such as PCBM, TiO_2, ZnO, C_{60}, IGZO, WS_2, and CeO_2 (Figure 1a). After selecting the most promising combinations, we further investigated the effects of the $CsSnI_3$ absorber and ETL thickness on the performance of the six best-performing devices in terms of PV parameters, series and shunt resistance, and operating temperature. Additionally, the impact of capacitance, Mott−Schottky (MS), generation and recombination rate, current−voltage (J−V) properties, and quantum efficiency (QE) were assessed. The acquired SC parameters are finally been compared with previous studies. To design and manufacture low-cost, high-efficiency, and lead-free $CsSnI_3$-based solar cells, six competitive and feasible designs for high-efficiency $CsSnI_3$ solar cells have been investigated thoroughly using a combination of SCAPS-1D and DFT computations.

2. MATERIALS AND METHODOLOGY

2.1. First Principal Calculations of $CsSnI_3$ Absorber Layer. In this study, first-principle calculations based on DFT were performed with CASTEP code to provide deep insights into the ground state configuration, optical, and electronic properties of bulk $CsSnI_3$ compound using $Pm\bar{3}m$ symmetry. In the total energy calculations, the exchange-correlation potential (E_{XC}) was treated in generalized gradient approximation (GGA) proposed by Perdew−Burke−Ernzerhof (PBE).[48,49] The interactions between electrons and nuclei were described with ultrasoft pseudopotentials of the Vanderbilt, which require a relatively smaller basis set and thus are computationally favorable.[50] The basis sets were expanded with an energy cut-off of 520 eV. Broyden−Fletcher−Goldfarb−Shannon (BFGS) algorithm was used to minimize the total energy and obtain the ground state properties. In reciprocal space, the Brillouin zone integration was performed with the Monkhorst−Pack (MP) scheme with a 12 × 12 × 12 k-points mesh for geometry optimization, whereas, to obtain reliable results, the electronic density of states and charge density calculations were carried out with a dense 17 × 17 × 17 k-mesh. The energy minimization iterations were carried on until the energy difference between two consecutive iterations becomes less than 10^{-4} eV. During the relaxation of atomic positions, the atoms were allowed to move under the critical force of 0.001 eV/Å and a stress of 0.05 GPa.

2.2. SCAPS-1D Numerical Simulation. To model perovskite PSCs, the ELIS department at the University of Gent developed the SCAPS-1D code. With the help of realistic and accurate back-end physical equations, a wide range of device architectures can be designed and investigated using the flexible PV software SCAPS 1D.[51−56] This software simulates photovoltaic processes like light absorption, exciton generation, charge transfer and collection, and recombination. Equation 1 defines Poisson's equation, which defines the relation between electrostatic potential and the charge density distribution.[57]

$$\frac{d^2}{dx^2}\psi(x) = \frac{q}{\varepsilon_0\varepsilon_r}[p(x) - n(x) + N_D - N_A + \rho_p - \rho_n] \tag{1}$$

In this equation, ψ stands for electric potential, ε_r is the relative permittivity, ε_0 stands for the permittivity of free space, $N_{D/A}$ are the densities of donors/acceptors, n/p refers to the electron/hole concentration, $\rho_{p/n}$ are the hole/electron charge density, and q is the electronic charge.

The continuity equations for electrons and holes are given by eqs 2 and 3, respectively:

$$\frac{\partial n}{\partial t} = \frac{1}{q}\frac{\partial J_n}{\partial x} + (G_n - R_n) \tag{2}$$

$$\frac{\partial p}{\partial t} = \frac{1}{q}\frac{\partial J_p}{\partial x} + (G_p - R_p) \tag{3}$$

In these equations, $J_{n/p}$ stands for the current densities of electrons/holes, $G_{n/p}$ are the electron/hole generation rates, and $R_{n/p}$ stands for the recombination rate for electrons/holes.

Charge carrier drift-diffusion is used to calculate both the electron and hole current densities in the PSC by using eqs 4 and 5:

$$J_n = q\mu_n n \in +qD_n\partial n \tag{4}$$

$$J_p = q\mu_p p \in -qD_p\partial p \tag{5}$$

In these equations, $D_{n/p}$ stands for the diffusion coefficient of electrons/holes, and $\mu_{n/p}$ stands for the mobility of charge carriers.

At contacts and interfaces, SCAPS-1D solves both Poisson's equation as well as continuity equations for the charge carriers. The FF of the device specified by eq 6 is[58]

$$FF = \frac{J_{mp} \times V_{mp}}{J_{SC} \times V_{OC}} \tag{6}$$

The terms V_{mp} and J_{mp} in this context refer to the maximum obtainable voltage and current density from the SC. The short-circuit current density is denoted by J_{SC}, and the open-circuit voltage is denoted by V_{OC}. Equation 7 illustrates the device efficiency normalized with respect to the power input P_{in} equivalent to the AM 1.5G spectrum.[59]

$$\eta = \frac{V_{OC} \times J_{SC} \times FF}{P_{in}} \tag{7}$$

2.3. $CsSnI_3$ Perovskite Solar Cell Structure. The study involved simulations of PSCs based on the $CsSnI_3$ absorber layer. In n−i−p planar structures, the ETL denotes the n-region, HTL constitutes, and the perovskite layer is located in the i-region. When the cell is illuminated, the perovskite i-layer generates an exciton, which is a Coulombic pair of an electron and a hole. When the exciton dissociates at the junction of the i- and p-layers, the hole moves to the p layer and the residual electron to the n layer. The electric field existing at the interface of two different layers speeds up the process of exciton dissociation.

https://doi.org/10.1021/acsomega.3c00306
ACS Omega 2023, 8, 22466−22485

Table 1. Input Parameters of TCO, ETL, and Absorber Layer ($CsSnI_3$)[60−62]

parameters	ITO	TiO_2	PCBM	ZnO	C_{60}	IGZO	WS_2	CeO_2	$CsSnI_3$
thickness (nm)	500	30	50	50	50	30	100	100	800[a]
band gap, E_g (eV)	3.5	3.2	2	3.3	1.7	3.05	1.8	3.5	1.3
electron affinity, X (eV)	4	4	3.9	4	3.9	4.16	3.95	4.6	3.6
dielectric permittivity (relative), ε_r	9	9	3.9	9	4.2	10	13.6	9	9.93
CB effective density of states, N_C ($1/cm^3$)	2.2×10^{18}	2×10^{18}	2.5×10^{21}	3.7×10^{18}	8.0×10^{19}	5×10^{18}	1×10^{18}	1×10^{20}	1×10^{19}
VB effective density of states, N_V ($1/cm^3$)	1.8×10^{19}	1.8×10^{19}	2.5×10^{21}	1.8×10^{19}	8.0×10^{19}	5×10^{18}	2.4×10^{19}	2×10^{21}	1×10^{18}
electron mobility, μ_n (cm^2/Vs)	20	20	0.2	100	8.0×10^{-2}	15	100	100	1.5×10^3
hole mobility, μ_h (cm^2/Vs)	10	10	0.2	25	3.5×10^{-3}	0.1	100	25	5.85×10^2
shallow uniform acceptor density, N_A ($1/cm^3$)	0	0	0	0	0	0	0	0	10^{20}
shallow uniform donor density, N_D ($1/cm^3$)	1×10^{21}	9×10^{16}	2.93×10^{17}	1×10^{18}	1×10^{17}	1×10^{17}	1×10^{18}	10^{21}	0
defect density, N_t ($1/cm^3$)	1×10^{15a}	1×10^{15a}	1×10^{15a}	1×10^{15a}	1×10^{15a}	1×10^{15a}	1×10^{15a}	1×10^{15a}	1×10^{15a}

[a]In this study, these values remain constant during initial optimization to get the best combination of HTL, ETL, and back metal contact.

Table 2. Input Parameters of Different HTLs[60]

HTL	Cu_2O	CuSCN	P3HT	PEDOT:PSS	Spiro-MeOTAD	NiO	CuI	CuO	CFTS	CBTS
thickness (nm)	50	50	50	50	200	100	100	50	100	100
band gap, E_g (eV)	2.2	3.6	1.7	1.6	3	3.8	3.1	1.51	1.3	1.9
electron affinity, X (eV)	3.4	1.7	3.5	3.4	2.2	1.46	2.1	4.07	3.3	3.6
dielectric permittivity (relative), εr	7.5	10	3	3	3	10.7	6.5	18.1	9	5.4
CB effective density of states, NC ($1/cm^3$)	2×10^{19}	2.2×10^{19}	2×10^{21}	2.2×10^{18}	2.2×10^{18}	2.8×10^{19}	2.8×10^{19}	2.2×10^{19}	2.2×10^{18}	2.2×10^{18}
VB effective density of states, NV ($1/cm^3$)	1×10^{19}	1.8×10^{18}	2×10^{21}	1.8×10^{19}	1.8×10^{19}	1×10^{19}	1×10^{19}	5.5×10^{20}	1.8×10^{19}	1.8×10^{19}
electron mobility, μn (cm^2/Vs)	200	100	1.8×10^{-3}	4.5×10^{-2}	2.1×10^{-3}	12	100	100	21.98	30
hole mobility, μh (cm^2/Vs)	8600	25	1.86×10^{-2}	4.5×10^{-2}	2.16×10^{-3}	2.8	43.9	0.1	21.98	10
shallow uniform acceptor density, N_A ($1/cm^3$)	1×10^{18}	1×10^{18}	1×10^{18}	1×10^{18}	1.0×10^{18}	1×10^{18}	1.0×10^{18}	1×10^{18}	1×10^{18}	1×10^{18}
shallow uniform donor density, N_D ($1/cm^3$)	0	0	0	0	0	0	0	0	0	0
defect density, N_t ($1/cm^3$)	1.0×10^{15a}	1×10^{15a}	1×10^{15a}	1×10^{15a}	1.0×10^{15a}	1×10^{15a}	1.0×10^{15a}	1×10^{15a}	1×10^{15a}	1×10^{15a}

[a]In this study.

Table 3. Input Parameters of Interface Defect layers[60]

interface	defect type	capture cross section: electrons/holes (cm^2)	energetic distribution	reference for defect energy level	total density (cm^{-2}) (integrated over all energies)
ETL/$CsSnI_3$	neutral	1.0×10^{-17} / 1.0×10^{-18}	single	above the VB maximum	1.0×10^{10}
$CsSnI_3$/HTL	neutral	1.0×10^{-18} / 1.0×10^{-19}	single	above the VB maximum	1.0×10^{10}

In the analysis, the TCO, back contact, and absorber were represented by the indium-doped tin oxide (ITO), Au (gold), and $CsSnI_3$, respectively (Table 1). Figure 1a illustrates the PSC architecture examined using 7 ETLs and 10 HTLs to determine the optimal pairing during simulation with SCAPS-1D. Potential ETL and HTL candidates (Tables 1 and 2) are carefully chosen based on outstanding characteristics like high mobility and suitable electronic affinity, which resolve the V_{OC} deficit issue caused by nonradiative recombination, which causes the unwanted quasi-Fermi level splitting phenomenon. In addition, an adequate ETL band gap boosts the photogenerated carrier rate, in addition to a long diffusion length, preventing J_{SC} saturation as perovskite material thickness increases. The interwoven effect of these parameters may hinder the performance of the SC. Our goal is to find the best charge transport materials that establish a compromise between electrical and optical outputs in order to improve solar cell performance. The addition of interface defect density at each of the junctions specified in Table 3 adds to the practicality of the simulations. To determine the impact of operating temperature on the PSC performance, simulations were run at an ambient temperature of about 300 K with an incoming power density and a frequency of 100 mW/cm^2 and 1 MHz, respectively, under the AM 1.5G solar spectrum.

3. RESULTS AND DISCUSSIONS

3.1. Analysis of DFT Results. *3.1.1. Structural Properties of $CsSnI_3$ Compound.* The $CsSnI_3$ perovskite phase has a cubic

https://doi.org/10.1021/acsomega.3c00306
ACS Omega 2023, 8, 22466−22485

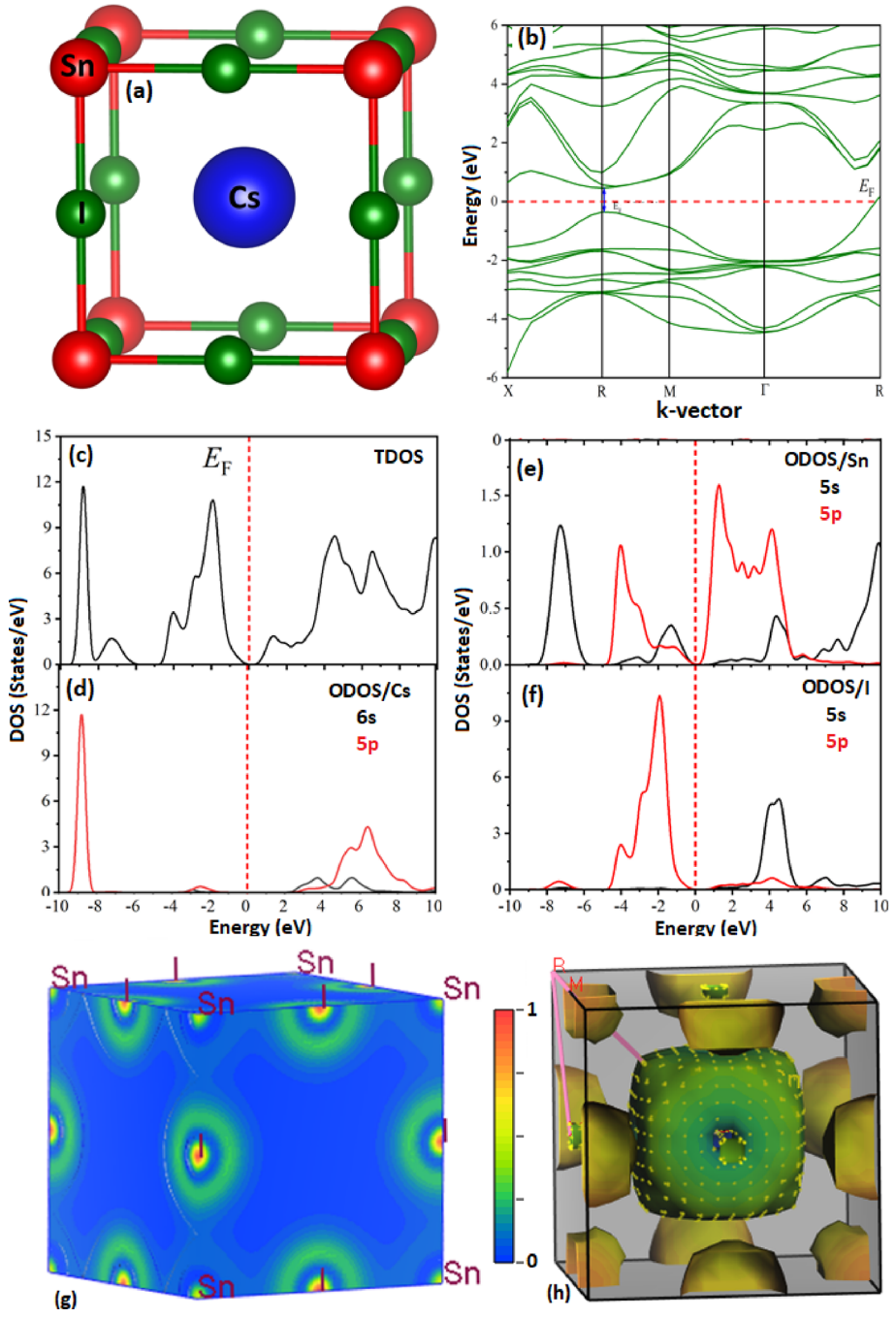

Figure 2. (a) Relaxed geometry, (b) band structure, (c–f) total and orbital density of states, (g) electronic charge density map, and (h) Fermi surface contour of $CsSnI_3$ perovskite.

structure (space group $Pm\bar{3}m$, no. 221) formed by the Cs, Sn, and I atoms with high symmetric atomic positions of (0.0, 0.0, 0.0), (0.50, 0.50. 0.50), and (0.00, 0.50, 0.50), respectively[63] (Figure 1b). The fully relaxed geometry of $CsSnI_3$ is shown in Figure 2a. It can be seen that the Cs atom is located in the middle of the unit cell; Sn atoms are positioned at the corners of the cube; and iodine atoms are present between the edges of Sn atoms. The Cs atom is placed at the octahedral position, surrounded by eight neighboring I atoms. The computed distance between Cs and I atoms is found to be 3.14 Å, and the I–Cs–I bond angle θ(I–Cs–I) is exactly 90°. The interatomic distance between Cs and Sn atoms d(Cs, Sn) is 5.44 Å, while the distance between Cs and I atoms d(Cs, I) is 4.44 Å. The Sn–Cs–Sn angle θ(Sn–Cs–Sn) is 70.52°, being shorter (larger) than the I–Cs–I angle θ(I–Cs–I) of 90°. The compound has a ground state total energy (E_0) of −1589.4673 eV, which yields the lattice constant (a) of 6.253 Å, close to the experimental value of 6.219 Å.[64] Additionally, the significant negative forming energy value (E_f = −1589.4673 eV/atom) of the optimized structure shows that it has a stable structural design that is appropriate for the construction of the solar system.

3.1.2. Electronic Properties of $CsSnI_3$ Compound. Based on the relaxed structure, the electronic properties of the $CsSnI_3$ perovskite are explored by computing the electronic band structure, density of states, charge density, and Fermi surface, as shown in Figure 2. From the band structure calculated along

https://doi.org/10.1021/acsomega.3c00306
ACS Omega 2023, 8, 22466–22485

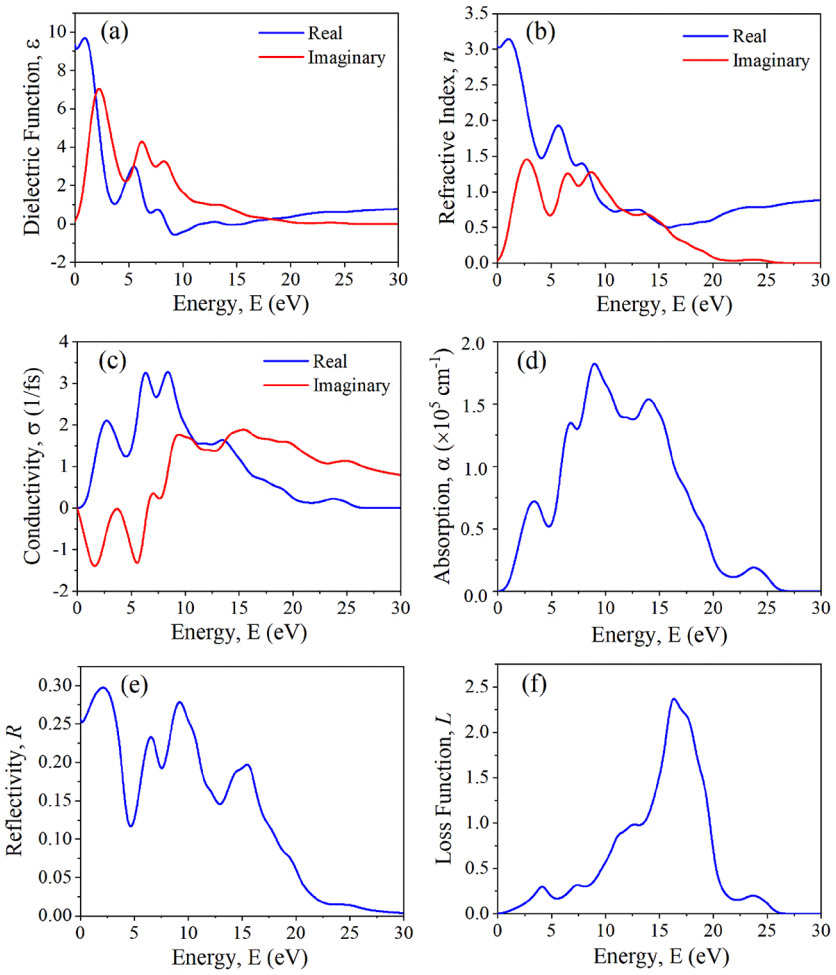

Figure 3. Calculated six optical functions ((a) dielectric function, (b) refractive index, (c) conductivity, (d) absorption, (e) reflectivity, and (f) loss function) of the $CsSnI_3$ perovskite solar absorber.

high symmetry k-points in the Brillouin zone (Figure 2b), it is obvious that $CsSnI_3$ is a direct band gap semiconductor, with valence band maximum (VBM) and conduction band minimum (CBM) located at the same value (R-point) of the k-vector in the Brillouin zone. The calculated band gap (E_g) is found to be 0.95 eV, slightly lower than the theoretically calculated E_g value of 1.307 eV reported elsewhere.[65] The formation of band structure can be examined with the density of states (DOS) plots shown in Figure 2c−f. In the total DOS (TDOS) shown in Figure 2c, there is no overlap of electronic states at the Fermi level, and it has a distinct separation between occupied and unoccupied energy states. Thus, TDOS also confirms that the given material has a band gap at the Fermi level, which is consistent with the band structure result. The atomic origin of the energy bands appearing within valence (conduction) bands can be probed by the analysis of partial and orbital DOS (that is lm-decomposed DOS) of the constituent atoms. In Figure 2d, it is found that the Cs atoms have no significant contribution to the formation of the band edges, and the Cs 5p sites are located far away from the Fermi level. However, the observed high-intensity peak in Figure 2d around −9 eV far below the Fermi level mainly originates from the Cs 5p valence electron states, while Cs 6s states have almost no obvious role in the construction of band edges. Conversely, the Sn 5s/5p states have a clear contribution to the electronic states forming the band gap. Thus, among the constituent Cs, Sn, and I atoms, the band gap is formed by the hybridization between the electronic states of Sn and I atoms.

3.1.3. Electron Charge Density of $CsSnI_3$ Compound. The electronic charge density plot (Figure 2g) along the (100) plane is used to predict the charge transformation behavior and nature of bonding among the constituent atoms, ions, or elements. Hence, to examine the electronic property of a material system more substantially, charge density distribution essentially depends on the electronic structure and density of states. This intricate characteristic displays a valence electron charge density figure and heavily depends on the calculation approach, premises, dimensions, and directions of the process concerned. The charge density output curves differ from structure to structure as well. The total electronic charge density map is examined in order to study the behavior of chemical bonding inside a compound. In essence, the charge density map/curve is made up of structural atoms/ions that show how orbital electrons contribute to the electrical characteristics of atoms/ions by collecting charges. Red and blue patterns stand for the high and low charge densities of the $CsSnI_3$ solar absorber, respectively. The fact that the majority of charges explicitly concentrate around I and that the distribution of charges is uniformly spherical about I suggests that the Sn−I bonds are quite stronger. Furthermore, the electron distributions of Cs, I, and Sn ions do not overlap or transmit any charge. The presence of ionic bonding in the particular perovskite is clearly

https://doi.org/10.1021/acsomega.3c00306
ACS Omega 2023, 8, 22466−22485

demonstrated by the charge density, which is mostly found at the individual lattice positions of Cs, Sn, and I atoms but not between them. The ionic nature of the molecule is related to the spherical charge distribution around all the atoms, which also displays metallic properties.[66,67] Interestingly, the reported electronic charge density of $CsSnI_3$ is the same in every crystalline plane, demonstrating the material's isotropic character.

3.1.4. Fermi Surface of $CsSnI_3$ Compound. The thermal, electrical, optical, and transport properties of a compound can be illustrated and predicted by its Fermi surface topology, and it can be derived from its electronic band structure.[68] The investigated Fermi surface topology at different paths of the Brillouin zone of the $CsSnI_3$ solar absorber is depicted in Figure 2h. From the figure, we found a rectangular benzene shape with a small hole at the center located at the hub $\Gamma(0.0,0.0,0.0)$ point, which acts as a hole-like surface. The center $\Gamma(0.0,0.0,0.0)$ point directly connects the $R(0.5,0.5,0.5)$ point of the corner that passes through a curved-shaped electron-like Fermi surface. The $R(0.5,0.5,0.5)$ point touches a separate small hole-like circular disc at the $X(0.0,0.5,0.5)$ point of the body center. Again, the R point slightly touches an adjacent curved shape electron-like Fermi surfaces at the $M(0.5, 0.0, 0.5)$ point of the topology. Therefore, both electron-like and hole-like Fermi surfaces are visualized, which is an implication of the multiband character of $CsSnI_3$. Also, it may be argued that electronic conductivity may be primarily caused by the highly dispersive band formed by the hybridization of the Sn 5p and I 5s orbitals.

3.1.5. Optical Properties of $CsSnI_3$ Compound. Analyzing the complex dielectric function is crucial to learn more about the optical behavior of compounds.[69] As a result, these characteristics are extremely important for investigating potential applications of substances in solar and optoelectronic devices. In this study, the nature of the calculated six optical parameters is ascribed in terms of energy up to 30 eV (Figure 3). To investigate how materials react to electromagnetic waves and how those waves spread via various media, complex dielectric functions are used. A dielectric function with the notation $\varepsilon(\omega) = \varepsilon_1(\omega) + i\varepsilon_2(\omega)$ can be used to calculate the optical response of any medium. Using the theoretical methodology, the real part $\varepsilon_1(\omega)$ and imaginary part$\varepsilon_2(\omega)$ of the dielectric function have been investigated for the compound $CsSnI_3$ as shown in Figure 3a.

The calculation of the zero-frequency limit, which is the electronic component of static dielectric constant $\varepsilon_1(0)$, is the most notable measurement of the real part of the dielectric function, $\varepsilon_1(\omega)$ as it firmly relies on the band gap of the compound. The value of $\varepsilon_1(0)$ computed from Figure 3a is about 9 eV. $\varepsilon_1(\omega)$ denotes the electronic polarizability of a particular material.[69] It is evident from the figure that the real part of the dielectric function comprises both negative and positive values. The propagation of electromagnetic waves is associated with the positive half, whereas their absorption is correlated to the negative half as the electromagnetic waves do not propagate in the compounds in this negative range. The highest peak of the $\varepsilon_1(\omega)$ is observed in the visible part of the electromagnetic spectrum, and the value abruptly starts reducing toward zero and eventually becomes negative from around ~6.5 eV, suggesting the maximum absorption in this negative range. A photon's absorption is related to the $\varepsilon_2(\omega)$, which represents the electronic characteristics of crystalline materials. The sharp peaks in the $\varepsilon_2(\omega)$ depict how charge carriers switch from filled to empty bands. $\varepsilon_2(\omega)$ exhibits significant values in the range from 0 to 10 eV, which indicates that the compound $CsSnI_3$ can be a prospective option for optoelectronic applications in the visible and UV region.

The refractive index (n) of a material is a crucial physical property that characterizes its optical characteristics. While the real part of the refractive index is linked with the phase velocity of the electromagnetic (em) waves in a particular medium, the imaginary part also known as the extinction coefficient quantifies the attenuation of the em waves traversing through the material.[70] Figure 3b portraying the refractive index displays a close resemblance with the real part of the dielectric function, as it is derived from $\varepsilon_1(\omega)$. The calculated static refractive index, $n(0)$ for the compound $CsSnI_3$ is about 3.02 having a sharp peak around 1 eV in the near IR region of the em spectrum, which further progress with higher energies to the visible and UV regions but with slightly lower values.

The ability of a medium to initiate a conduction phenomenon as em radiations try to propagate through at optical frequencies is determined by its optical conductivity $\sigma(\omega)$. It can be computed from the complex dielectric function.[69] It is obvious from the plot given in Figure 3c that conductivity rises with the increase in energy up to around 9 eV, and beyond this energy range, the conductivity decreases having a short oscillatory phase and eventually becomes static. The increased value of the $\sigma(\omega)$ in the visible and the UV regions can be attributed to the increase in absorption coefficient in this energy range as given in Figure 3d.

An essential optical function for using Kramers−Kroning relationships to determine all optical coefficients is the energy-dependent reflectance spectrum (R). In $CsSnI_3$ solar absorber material, which has an initial greater reflectivity than isostructural $CsSnCl_3$ (Figure 3e), the reflectivity spectrum starts at around 0.25 at zero frequency. Thereafter, R rapidly increases until it reaches its maximum value of 0.3 for a photon energy of around 2.60 eV. The maximum degree of reflectivity in the UV region in Figure 3e may have been caused by interband transitions. In addition, three distinct steep peaks may be seen at energies of 6.1, 9.7, and 15.1 eV. The maximal reflectance of $CsSnI_3$ (0.3) is lesser than that of $CsSnCl_3$ (0.41), which may be due to the difference in the electronic states of these two materials.

Figure 3f depicts the loss spectrum (L) of $CsSnI_3$, which shows how much energy a fast electron loses while traveling through a compound. The energy loss function only explains how electrons lose energy as a result of electron−matter interaction.[69] It can be observed that energy loss gradually increased showing maxima at a photon energy of 14.8 eV, with a few minor peaks. Then, it quickly accelerated, reaching its peak energy loss (2.3), also known as plasma frequency (p), at around 16.2 eV. It is obvious that the majority of energy loss occurs in the UV spectrum due to the greater photon energy than that of the band gap energy.

3.2. Analysis of SCAPS-1D Results. In this section, the PV response of the heterostructure ITO/ETL/$CsSnI_3$/HTL/Au is assessed by varying the ETL, absorber, and HTL layers while maintaining the respective thickness for HTL given in the parentheses (Cu_2O (50 nm), CuSCN (50 nm), P3HT (50 nm), PEDOT:PSS (50 nm), Spiro-MeOTAD (50 nm), NiO (50 nm), CuI (50 nm), CuO (50 nm), CFTS (50 nm), and CBTS (50 nm)) and ETL (PCBM (50 nm), ZnO (50 nm), C_{60} (50 nm), IGZO (30 nm), WS_2 (100 nm), and CeO_2 (100 nm)) for the 800 nm $CsSnI_3$ absorber layer constant, and the acceptor concentration and defect densities are set at 10^{18} cm^{-3} and 10^{15}

https://doi.org/10.1021/acsomega.3c00306
ACS Omega 2023, 8, 22466−22485

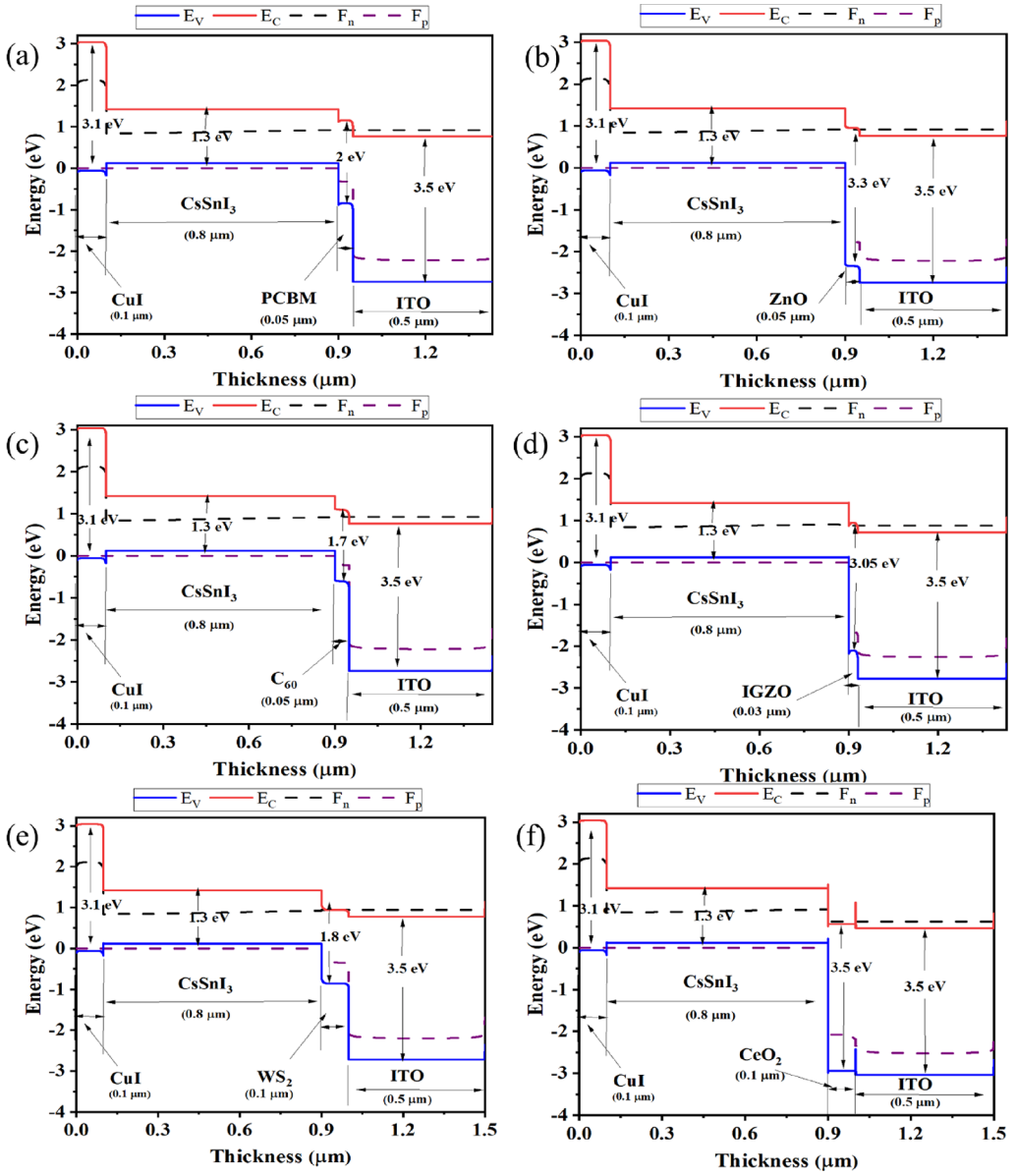

Figure 4. EBD of $CsSnI_3$-based PSC with CuI HTL, Au back contact, and different ETLs: (a) PCBM, (b) ZnO, (c) C_{60}, (d) IGZO, (e) WS_2, and (f) CeO_2.

cm^{-3}, respectively. After the initial simulation, based on the performance of 70 different combinations, the best-performing devices were investigated through different studies discussed in the following sections.

3.2.1. Energy Band Diagram (EBD) of $CsSnI_3$. Each studied ETL with a $CsSnI_3$ PAL and CuI as HTL influence the valence/conduction band offset in the EBD (difference of VBM between the HTL and the absorber layer and CBM between the absorber layer and ETL). Energy level alignment has a substantial impact on the efficiency and performance of PSCs. Photogenerated electrons are injected into the ETL conduction band, whereas holes are transferred to the CuI HTL in PSCs. Following that, electrons and holes are collected at their respective front (ITO) and back (Au) contact metals. However, the electron affinity of each ETL (PCBM, ZnO, C_{60}, IGZO, WS_2, and CeO_2) should be greater than that of $CsSnI_3$ to extract the electron at the ETL/$CsSnI_3$ interface, and the ionization energy of CuI HTL should be lower than that of $CsSnI_3$ to extract the holes at the $CsSnI_3$/CuI HTL interface. Furthermore, energy band mismatches at each of the ETL/$CsSnI_3$ and $CsSnI_3$/CuI HTL interfaces have a considerable impact on device PV performance parameters such as J_{SC}, V_{OC}, FF, and PCE. The Fermi level is uniform throughout the entire structure under thermal equilibrium conditions, and the incidence of photons on the PSC structure disturbs this alignment with the formation of quasi-Fermi energy levels. When the CBM of the ETL lies above the CBM of the absorber (positive CBO), a spike is formed at the ETL/absorber interface, which blocks the electron flow. However, a smooth flow of electrons is ensured in the opposite case of negative CBO.[71] On the other hand, for effective hole transport, the VBM of the HTL should be greater than that of the perovskite. The activation energy for recombination is defined as $E_a = E_g - |CBO/VBO|$, and the recombination increases with decreasing E_a due to higher CBO/VBO.[72] From the EBDs, shown in Figure 4a–f, it can be observed that the VBO at the HTL/perovskite interface is small enough for efficient hole transport. Devices with PCBM as the ETL and CuI as HTL exhibit the best PCE of 10.10% due to its smaller CBO, which helps in efficient electron transport as

https://doi.org/10.1021/acsomega.3c00306
ACS Omega 2023, 8, 22466−22485

compared to the other ETLs (Figure 4a). Almost similar values of CBO are also obtained with ETLs C_{60} and WS_2 (Figure 4c,e). However, somewhat inferior PV performance is achieved with ZnO, IGZO, and CeO_2 as ETL and CuI as HTL due to higher CBO, thereby leading to increased recombination and low efficiency (Figure 4b,d, f) The worst-case scenario is observed with CeO_2, which shows the highest CBO and the lowest efficiency of 6.23%.

3.2.2. Effect of ETL. In this study, a $CsSnI_3$-based PSC was studied, with 7 ETLs, 10 HTLs, and Au as the back metal contact initially. Utilizing the SCAPS-1D platform, 70 different configurations of SCs are tested numerically to see how well they work, and six sets of optimized SCs are reported. To find the best ETL/HTL combination, 70 different SC configurations are tested with each of the ETL enlisted in Table 1 and distinct HTL from Table 2. Based on Table 4, it was apparent that the six best-performed structures were taken from 70 possible combinations. Figure 5 illustrates PV characteristics for all the $CsSnI_3$-based configurations while Figure 5a shows V_{OC} for all studied ETLs and HTLs. Among the studied ETLs, WS_2 ETL showed the highest V_{OC} of 0.933 V and CeO_2 ETL showed the lowest V_{OC} of 0.553 V. ETLs like PCBM, TiO_2, ZnO, and C_{60} showed similar kinds of V_{OC} ranges from 0.909−0.913 V for the most number of cases. From Figure 5b, it can be seen that among all devices, J_{SC} values of 15.9 and 0.298 mA/cm^2 of CeO_2 ETL were the highest and lowest for all the ETL and HTL configurations investigated. For all the $CsSnI_3$ combinations, the maximum range of FF was between ∼45 and 78 and ∼44 and 76% for PCBM and IGZO ETLs, respectively, while CeO_2 ETL showed the minimum FF range between ∼39 and 65%. PCBM ETL showed maximum throughput with all the HTLs. In the ITO/ETL/$CsSnI_3$/HTL/Au heterostructure, ETLs like PCBM, C_{60}, and WS_2 resulted in comparatively better efficiency in the range of ∼9−10%. On the other hand, ZnO, IGZO, TiO_2, and CeO_2 performance was not satisfactory with an efficiency of ≤8%.

Table 4. PV Parameters for the Best Configuration for each of the ETLs

optimized device	V_{OC} (V)	J_{SC} (mA/cm^2)	FF (%)	PCE (%)
ITO/PCBM/$CsSnI_3$/CuI/Au	0.909	14.24	78.11	10.1
ITO/ZnO/$CsSnI_3$/CuI/Au	0.913	12.01	72.76	7.97
ITO/C_{60}/$CsSnI_3$/CuI/Au	0.909	14.81	69.99	9.43
ITO/IGZO/$CsSnI_3$/CuI/Au	0.865	11.63	73.09	7.35
ITO/WS_2/$CsSnI_3$/CuI/Au	0.933	13.59	73.08	9.26
ITO/CeO_2/$CsSnI_3$/CuI/Au	0.603	15.86	65.06	6.23

3.2.3. Effect of HTL. Ten different HTLs were used in this analysis to evaluate seven sets of ETLs. Except for TiO_2, all of the ETL alternatives performed better with the CuI HTL by about 6−10%. The HTLs like CuSCN, NiO, P3HT, PEDOT:PSS, Spiro-MeOTAD, CBTS, and CFTS also appear to be most matched with the $CsSnI_3$ absorber when evaluated from the performance point of view (Figure 5). With regards to the other HTLs, the Cu_2O, and CuO HTLs underperformed when combined with each ETL. The HTL must be thicker and equal to the n-type ETL since studied HTLs are p-type layers in order to reduce the likelihood of recombination mainly because it enables the prompt transfer of an equivalent amount of charge carriers to the structure. Under these circumstances, the thickness of each ETL was chosen to be either lower or equal to the corresponding CuI HTL. Inorganic CuI is one of the most promising inorganic semiconductors for employment as HTL in PSCs to improve PV capabilities.[73,74] Due to its optimum band gap, high absorption coefficient, remarkable conductivity, and reduced valence band offset, which is good for hole transport, hydrophobicity, environmental stability, solution processability, nontoxicity, and naturally occurring abundance, the p-type semiconductor CuI can be used as a promising component for being used as an efficient HTL.[75] SCs utilize CuI as HTL, leading to greater stability and less hysteresis. Moreover, CuI is less expensive than Spiro-MeOTAD, making it an appealing option for reducing the cost of lead-free PSC manufacturing.

3.2.4. Effect of Absorber and ETL Thickness on PV Performance. In this subsection, the contour plot representation is used to examine the impact of the $CsSnI_3$ absorber layer with the six best-chosen ETL layer thicknesses on the PV performance of the PSC configurations. The fundamental and most important factor in producing high-performance SCs is to select a proper combination of an absorber and ETL. Additionally, the right absorber thickness with ETL contributes to the proper light harvesting and carrier transport from the perovskite absorber layer.

Figure 6 depicts how the ETL and absorber layer thickness of the six best-performed PSC structures mentioned in Table 4 affect the V_{OC} characteristics. In the case of PCBM, it can be seen from Figure 6a that the absorber thickness and ETL thickness of ≤0.1 and ≤ 0.2 μm, respectively, deliver a maximum V_{OC} of 0.918 V. With the increase in the ETL and absorber layer thicknesses, V_{OC} degrades. According to Figure 6b,c, ETLs ZnO and C_{60} showed a similar trend as that of PCBM achieving maximum V_{OC} 0.922 V for lower absorber layer thicknesses of 0.1 and 0.2 μm and ETL thicknesses of 0.01 and 0.03 μm, respectively. Maximum V_{OC} was achieved for the IGZO ETL-based structure with absorber and ETL thicknesses of less than 0.1 and 0.2 μm, respectively (Figure 6d). However, from Figure 6e, a somewhat different pattern is observed with WS_2 ETL, where higher V_{OC} values can be achieved with an absorber thickness less than 0.1 μm and ETL thickness in the range of 0.2−0.4 μm. In the case of CeO_2 (Figure 6f), the pattern of the variation in V_{OC} is similar to that of ZnO but the range of values of V_{OC} is much smaller as compared to the other ETLs. So, it can be concluded that higher V_{OC} can be achieved with lower thicknesses of the absorber and ETL, and the increase in thickness of these layers can lead to reduced PV performance.

The effect of changing the ETL and absorber layer thickness on the J_{SC} characteristics of six studied PSCs is shown in Figure 7. When the ETL thickness is between 0.03 to 0.15 μm and the absorber thickness is 0.2 to 0.3 μm for the PCBM-based ETL structure, the highest J_{SC} value of 14.80 mA/cm^2 is observed (Figure 7a). ZnO and IGZO ETL-based SCs exhibit a nearly identical pattern, with almost a similar highest J_{SC} of 15 and 14.94 mA/cm^2 when the absorber thickness and ETL thickness are 0.2 and 0.01 μm, respectively (Figure 7b,d). For the C_{60} ETL-based structure, a maximum J_{SC} value of 15.40 mA/cm^2 was demonstrated for ETL and absorber thicknesseses less than 0.15 and 0. 0.2 μm, respectively (Figure 7c). When the absorber thickness lies in the range 0.2−0.3 μm and WS_2 and CeO_2 thicknesses were 0.05 and 0.25 μm, respectively, the structures exhibited a maximum J_{SC} of ∼16.4 mA/cm^2, (Figure 7e,f). It is evident from the plots that lower thicknesses of the absorber and ETL are desirable for better performance.

Figure 8 depicts the degree of variation of FF with the change in the thickness of the absorber and ETL layers for the six

https://doi.org/10.1021/acsomega.3c00306
ACS Omega 2023, 8, 22466−22485

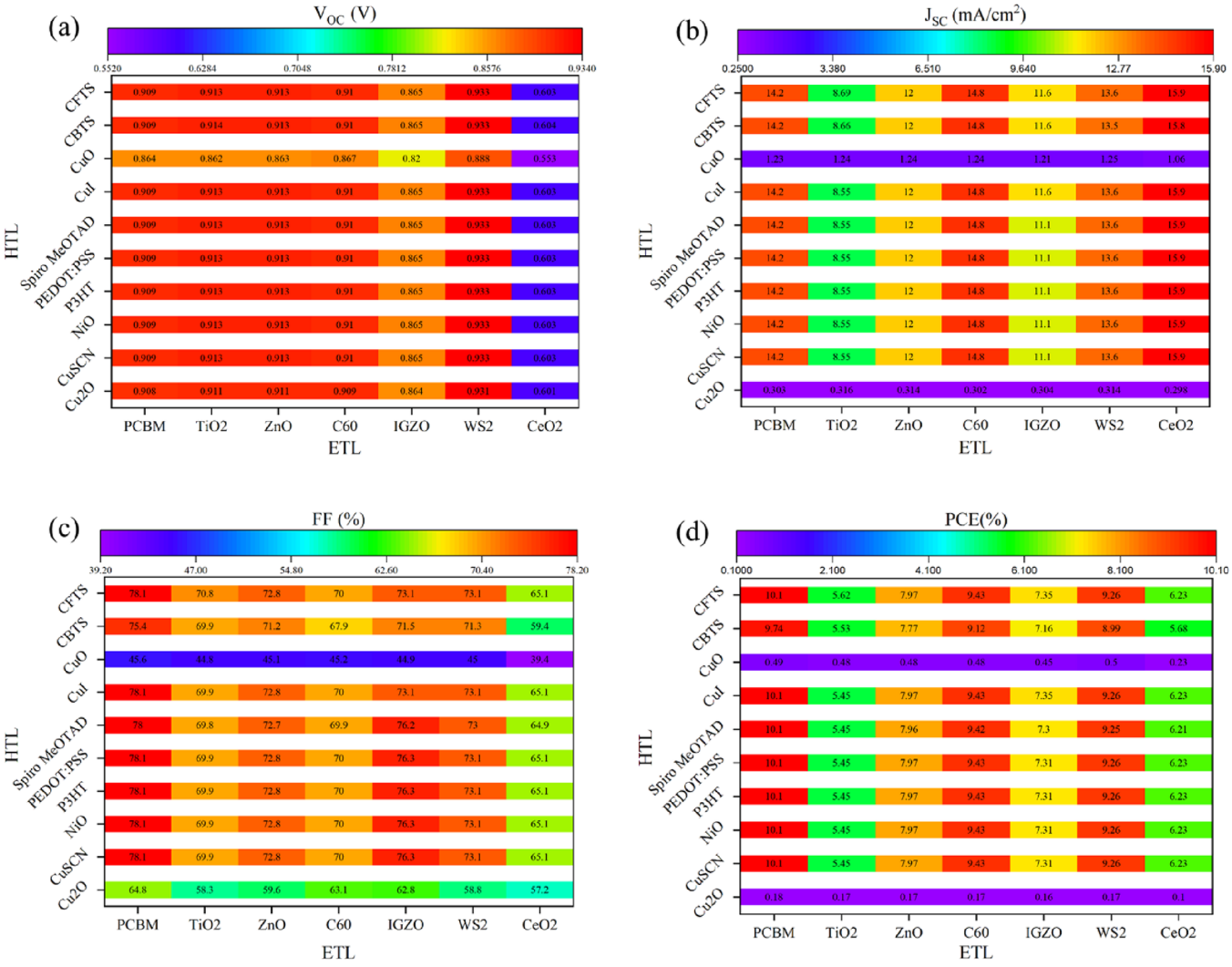

Figure 5. Variation of PV parameters (a) V_{OC} (V), (b) J_{SC} (mA/cm^2), (c) FF (%), and (d) PCE (%) of the $CsSnI_3$-based solar cell for the studied HTLs with Au as back contact and different ETLs.

devices under consideration. Figure 8a illustrates that for the PCBM ETL-based structure, FF values can drop from 83.10 to 75.50% ETL thickness in the range of 0.15−0.2 μm irrespective of the absorber thickness. For ZnO and CeO_2-based ETLs, it can be observed from Figure 8b,f that higher values of FF can be observed for absorber layer thicknesses below 0.2 μm. For CeO_2, the FF is almost independent of the thickness of the ETL and for ZnO, it can be observed that there is the least variation in FF for ETL and absorber thicknesses beyond 0.1 and 0.2 μm, respectively. C_{60} being a polymer almost shows the same pattern of variation in FF as that of PCBM, though the maximum value of FF achieved with this ETL is almost 2.8% lower than that of PCBM (Figure 8c). From the contour plots in Figure 8d,e, it can be concluded that for the ETLs IGZO and WS_2, high FF values can be achieved for ETL thicknesses beyond 0.15 μm irrespective of the absorber thickness.

The PSCs incorporated with PCBM and C_{60} ETL exhibited the same trend of PCE with rising absorber and ETL layer thickness, as shown in Figure 9a,c. When the absorber layer and the ETL thickness were 0.2 and 0.05 μm, PCBM and C_{60} ETL-based structures had the same maximum PCE of 10.80%. ETL ZnO and IGZO-based structures showed a similar trend of performance with PCEs of about 8.89 and 8.26%, while absorber and ETL thicknesses were 0.2 and 0.01 μm, respectively (Figure 9b,d). Among all the structures, WS_2 showed the highest PCE of 11.90% when absorber and ETL thicknesses were 0.2 and 0.3 μm (Figure 9e), while CeO_2 showed the lowest PCE of 6.51% with absorber and ETL thicknesses of 0.2 and 0.03 μm, respectively (Figure 9f). So, with the increment of the absorber and ETL thickness, PV parameters tend to decline, which is consistent with the previous studies.

3.2.5. Effect of Series Resistance. Shunt (R_{SH}) and series (R_S) resistances, which are mostly created by connections between the different layers of PSCs, metal contacts, semiconductor−metal interface, and faulty SC processing steps, have a major negative impact on the performance of perovskites. In the instance of ITO/ETL/$CsSnI_3$/CuI/Au devices, Figure 10 demonstrates the variation of different PV parameters due to the change in R_S from 0 to 6 Ω cm^2, with the shunt resistance kept constant at 10^5 Ω cm^2. It can be observed from Figure 10a,b that V_{OC} and J_{SC} are almost independent of R_S for different ETLs. While the highest V_{OC} is exhibited by WS_2, the lowest value occurs in the case of CeO_2. The highest and lowest values of J_{SC} are shown by CeO_2 and IGZO, respectively. However, the FF of the different devices are affected strongly by R_S and as a result of this, a similar variation is observed in the case of PCE also

https://doi.org/10.1021/acsomega.3c00306
ACS Omega 2023, 8, 22466−22485

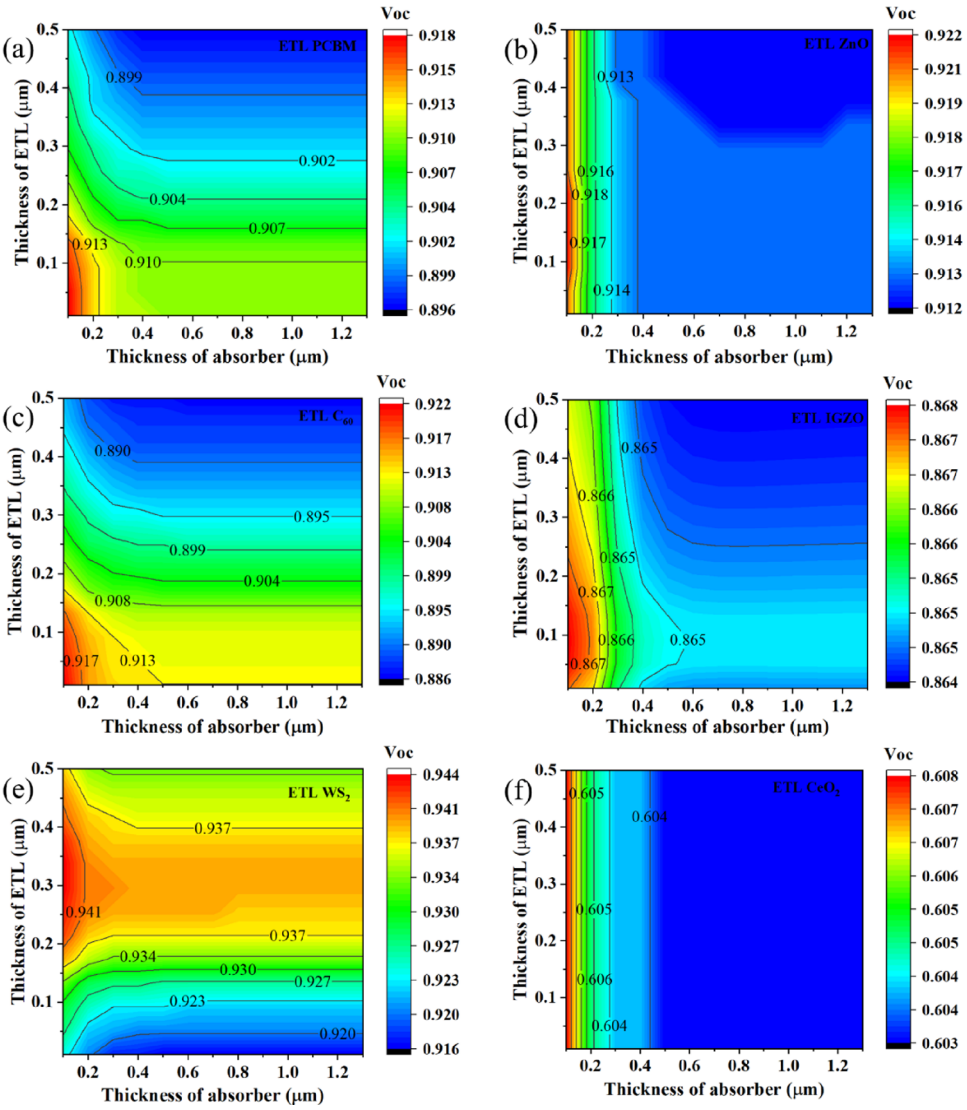

Figure 6. Contour plots showing the change in V_{OC} for $CsSnI_3$-based structures with (a) PCBM, (b) ZnO, (c) C_{60}, (d) IGZO, (e) WS_2, and (f) CeO_2 ETLs along with the simultaneous variation in ETL and absorber layer thicknesses.

(Figure 10c,d). In comparison with other structures, the ITO/CeO_2/$CsSnI_3$/CuI/Au PSC structure showed comparatively subpar V_{OC}, FF, and PCE performance, in spite of demonstrating the highest J_{SC}.

3.2.6. Effect of Shunt Resistance. In Figure 11a–d, we have investigated the effect of the variation in R_{SH} from 10–10^7 Ω cm^2 and a constant R_S of 0.5 Ω cm^2 on the PV parameters for ITO/ETL/$CsSnI_3$/CuI/Au heterostructure. It can be observed that the PV parameters V_{OC}, FF, and PCE are dependent on R_{SH}, but J_{SC} is almost independent of the variation in R_{SH} (Figure 11b). As R_{SH} rises from 10 and 10^3 Ω cm^2, V_{OC} increases sharply from 0.12 to 0.93 V, FF from 15 to 76%, and PCE from 0 to 10% except for the CeO_2 ETL-based structure. After this increment, beyond an R_{SH} of 10^4 Ω cm^2, the PV parameters were stable. It is believed that manufacturing flaws are the principal cause of the origin of R_{SH}. After a certain R_{SH} threshold is reached, the p-n junction offers a low-resistance channel for junction current flow.[60] In a previous report, we observed that V_{OC} rose on increasing shunt resistance up to 10^3 Ω cm^2, while J_{SC} remained almost unchanged.[60] As a result, obtaining the greatest PCE in an ITO/ETL/$CsSnI_3$/CuI/Au PSCs heterostructure requires an R_{SH} value of 10^4 Ω cm^2.

3.2.7. Effect of Temperature. PSCs have generated a lot of attention in the PV area, but when exposed to light often, they still exhibit thermal instability.[76] For instance, PSC performance will degrade by 10% after just 1000 h of operation at 85 °C, which is a significantly shorter period than the lifetime of silicon SCs.[77] In addition, the temperature can be used as a treatment for different layers, or PSCs as a whole while being used as the environment temperature for the simulation studies. Consequently, for future commercial use, it is necessary to clarify the temperature effect on PSCs considering variable values.

Figure 12 illustrates the effects of temperature fluctuations from 275 to 475 K on the performance benchmarks (V_{OC}, J_{SC}, FF, and PCE) for the six devices under the illumination of 1000 Wm^{-2} of solar light. For all devices, V_{OC} declines with the increase in temperature due to the increase in reverse saturation current except the CeO_2 ETL-based device, which showed an almost constant and the lowest V_{OC} for the entire temperature range. However, the J_{SC} of the structures showed an increment due to the increase in the temperature except for WS_2 ETL, which delivered a constant J_{SC} of 13.5 mA/cm^2. This increase in J_{SC} is due to the lowering of band gap with temperature, which

https://doi.org/10.1021/acsomega.3c00306
ACS Omega 2023, 8, 22466–22485

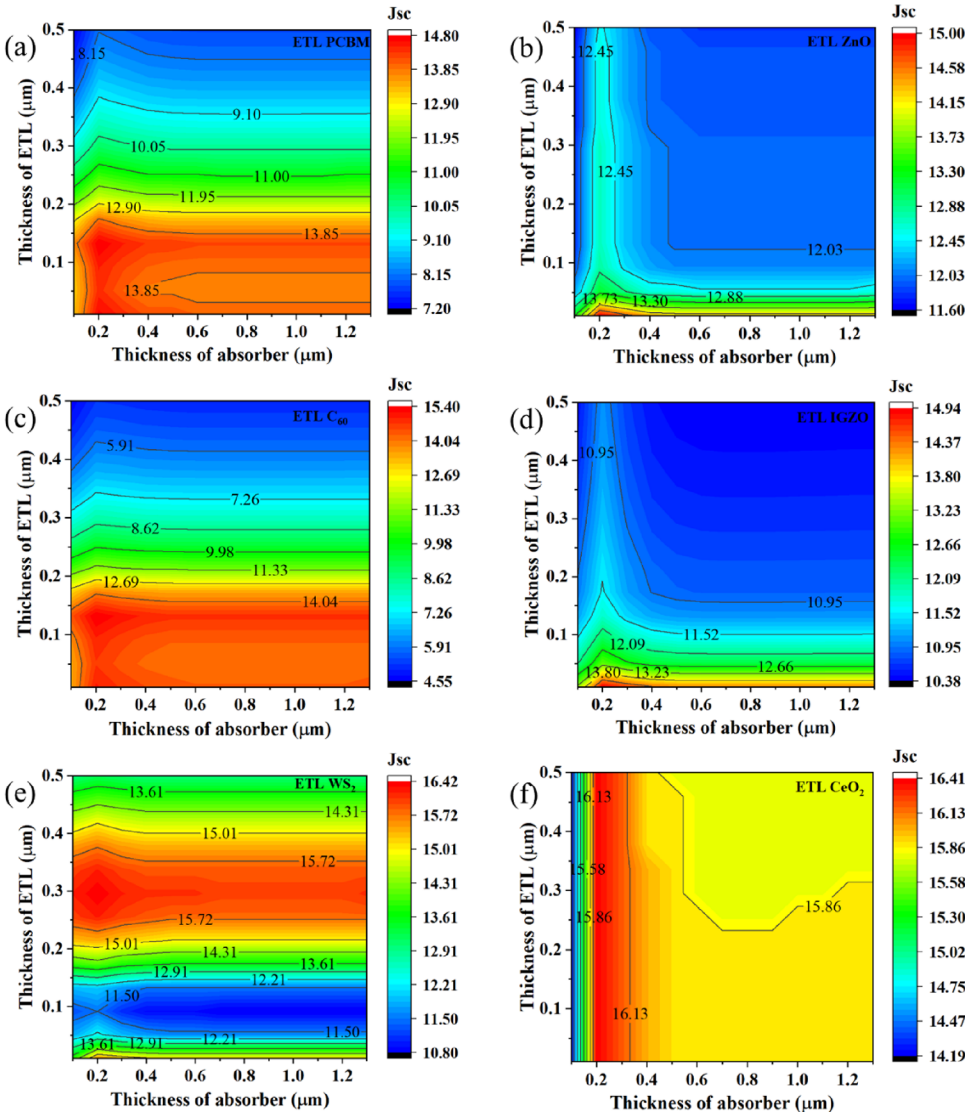

Figure 7. Contour plots showing the change in J_{SC} for $CsSnI_3$-based structures with (a) PCBM, (b) ZnO, (c) C_{60}, (d) IGZO, (e) WS_2, and (f) CeO_2 ETLs along with the simultaneous variation in ETL and absorber layer thicknesses.

enhances the electron−hole pair generation.[78,79] Equations 8 and 9 relate how V_{OC} relies on temperature:

$$V_{OC} = \frac{nKT}{q}\log\left(\frac{J_{SC}}{J_O} + 1\right) \tag{8}$$

$$\frac{d(V_{OC})}{dT} = \frac{V_{OC}}{T} - \frac{\frac{Eg}{q}}{T} \tag{9}$$

J_O, T, Eg, q, n, and k stand for the reverse saturation current, temperature, band gap, electronic charge, ideality factor, and Boltzmann constant, respectively.

FF for all the devices tends to increase up to 350 K and gradually declines thereafter with the increase in temperature. On the contrary, the PCE of all devices decreases except CeO_2 ETL-based devices while the temperature rises.

3.2.8. Effect of Capacitance and Mott-Schottky. Figure 13a−f illustrates the effect of capacitance and Mott−Schottky obtained with the help of $C-V$ analysis with a constant frequency of 1 MHz for six various configurations of $CsSnI_3$-based perovskites SCs with different ETLs. In Figure 13a−f, as the supply voltage goes up, the capacitance increases exponentially until it reaches saturation. Among all the studied devices, the CeO_2 ETL-based structure had the maximum capacitance at 9000 C (nF/cm^2), while C_{60} ETL-based structure showed the minimum capacitance. Except for CeO_2, the other devices show very low values of capacitance. When there is no bias, the device is in a depletion state, but when a forward bias of around 0.5 V is applied, the depletion width reduces to a value that is almost equal to the thickness of the absorber layer. So, as the forward bias voltage increases, the capacitance goes up, and the Mott−Schottky (MS) relationship stays the same.

Figure 13a−f demonstrates that among all the studied devices, C_{60} ETL-based structure had the maximum MS value of 0.00017 1/C^2, while the CeO_2 ETL-based structure showed the minimum MS value. The broadly used MS technique can be employed to figure out the built-in potential (V_{bi}), which shows the difference between electrode operation and doping level. The primary focus of the MS concept is on the properties of the p-n junction, where the intercept point on the x-axis of the $C-V$ curve usually corresponds to the V_{bi} of the corresponding junction, whereas the intercept point of the $1/C^2-V$ curve

https://doi.org/10.1021/acsomega.3c00306
ACS Omega 2023, 8, 22466−22485

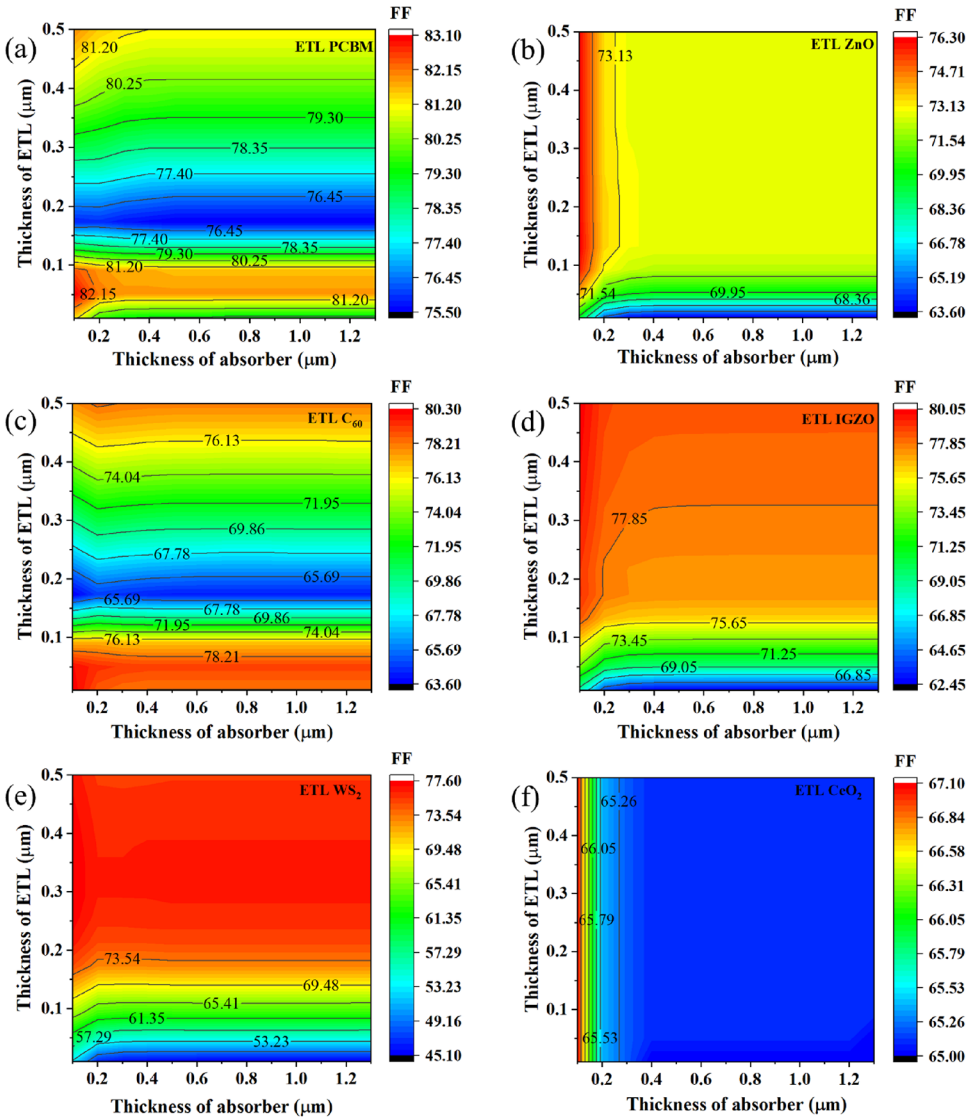

Figure 8. Contour plots showing the change in FF for $CsSnI_3$-based structures with (a) PCBM, (b) ZnO, (c) C_{60}, (d) IGZO, (e) WS_2, and (f) CeO_2 ETLs along with the simultaneous variation in ETL and absorber layer thicknesses.

signifies the concentration of occupied trapping centers. When the V_{bi} values go up, the MS values go down for that device. Here, the simulated results for all of the important criteria for each device were the same, and so they were comparable and in line with the findings reported in earlier reports.[80,81] The V_{bi} values reported in Figure 13a−f are obtained with the help of linear fitting in the portion obeying Mott−Schottky behavior and getting the intersection of the $(1/C^2)$ line with the horizontal axis. This method is in accordance with the publications reported in past.[82−85] The generation and recombination rate profiles are also depicted in Figure 14a,b.

3.2.9. Effect of Generation and Recombination Rate. Figure 14a,b demonstrates the carrier generation and recombination rates for $CsSnI_3$-based six PSCs over a depth of 0.0−1.5 μm, where the other input parameters were identical to the initial one. The results show that of all the studied devices, generation rates reach their highest point between 0.9 and 1.0 μm, and ITO/ZnO/$CsSnI_3$/CuI/Au had the maximum generation rate among all devices. SCAPS-1D uses the arriving photon flux $N_{phot}(\lambda, x)$ to figure out how many electron−hole pairs contribute to $G(x)$, and eq 10 uses this photon flux to figure out the value of $G(x)$ for each spectral region and position.

$$G(\lambda, x) = \alpha(\lambda, x) \times N_{phot}(\lambda, x) \tag{10}$$

On the other hand, the recombination rate is the opposite of the generation rate, which annihilates the generated electron−hole pairs and they cannot contribute to the photocurrent. The density and longevity of the charge carriers affect the rate of recombination in PSCs. The defect states in the absorber layer as well as the interfaces cause the enhancement in electron−hole recombination. All of the devices studied had their best recombination rates between 0.9 and 1.0 μm, but ITO/C_{60}/$CsSnI_3$/CuI/Au ETL had the greatest recombination peak. The energy levels created in the middle of the valence-conduction band mostly contribute to the recombination losses. The recombination rate distribution of PSCs can be uneven due to grain boundaries and shortcomings that form when junctions and structures are made.[81]

3.2.10. J−V and QE Characteristics. For device configurations ITO/ETL/$CsSnI_3$/CuI/Au, Figure 15 shows the current density−voltage $(J-V)$ characteristics and quantum

https://doi.org/10.1021/acsomega.3c00306
ACS Omega 2023, 8, 22466−22485

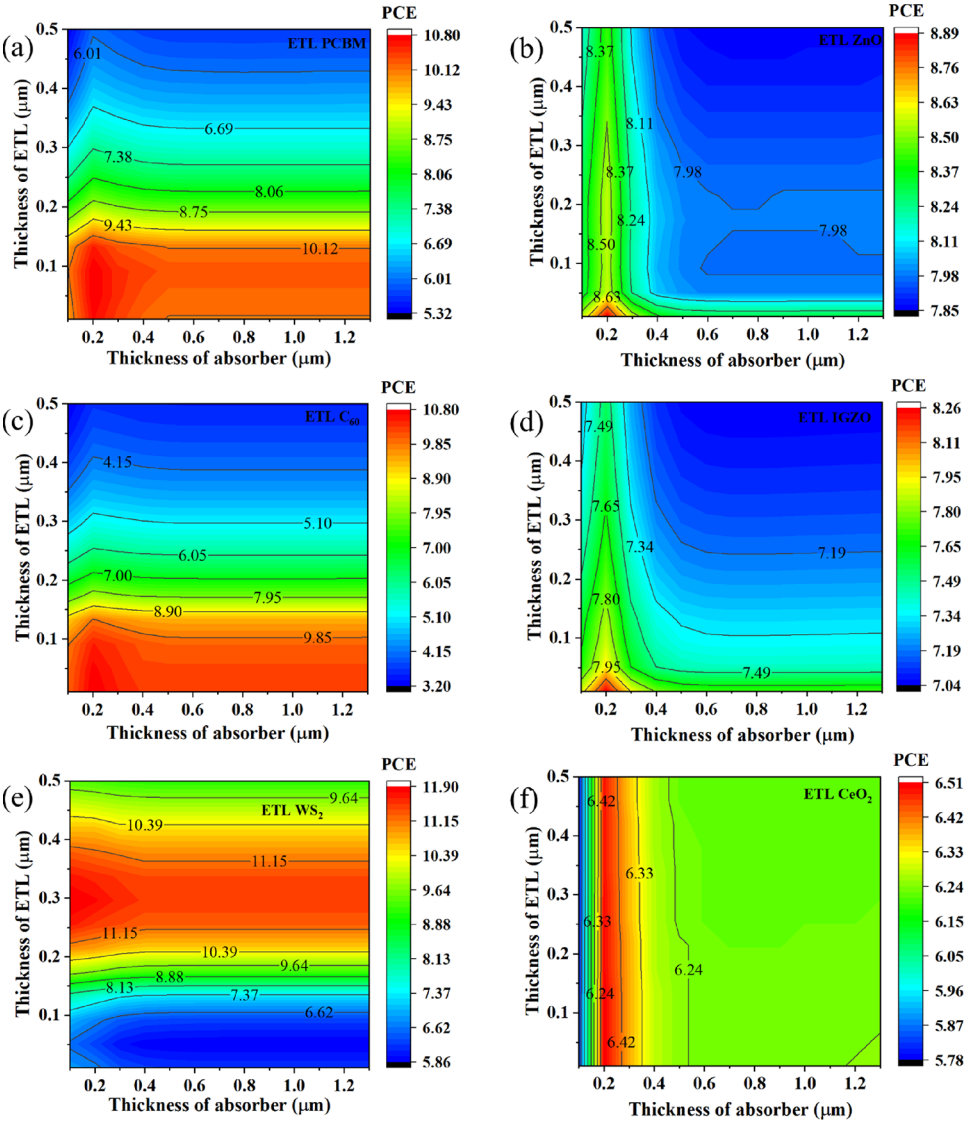

Figure 9. Contour plots showing the change in PCE for $CsSnI_3$-based structures with (a) PCBM, (b) ZnO, (c) C_{60}, (d) IGZO, (e) WS_2, and (f) CeO_2 ETLs along with the simultaneous variation in ETL and absorber layer thicknesses.

efficiency (QE) for six different ETLs. While ITO/CeO_2/$CsSnI_3$/CuI/Au produces the highest photocurrent, ITO/IGZO/$CsSnI_3$/CuI/Au delivers the lowest amount of photocurrent, which is the reason behind the higher amount of current density generated by the CeO_2 ETL. The flow of photogenerated in $CsSnI_3$-based PSCs is thus influenced by the ETL band structure, which is identical to previous results.[80] Though CeO_2 delivers the maximum photocurrent, it shows the lowest V_{OC}, which results in a reduction in PCE significantly. The lower value of V_{OC} is due to the higher electron affinity of CeO_2.

Figure 15b illustrates the correlation between quantum efficiency (QE) and wavelength (λ) in a wavelength range of 300−1000 nm. This QE began to peak at a wavelength of 300 nm and fell to 950 nm at the band edge of each active substance. Following the trend of $J-V$ characteristics, the QE was determined to be maximum for the ITO/WS_2/$CsSnI_3$/CuI/Au structure and minimum for the ITO/CeO_2/$CsSnI_3$/CuI/Au configuration. Because of the increased photon absorption in the $CsSnI_3$ absorber made possible by the lower band gap (~1.8 eV) of WS_2, a higher QE is produced. CeO_2 ($Eg \approx 3.5$ eV), on the other hand, has a higher band gap (~3.5 eV), which lowers the amount of passing photons that are absorbed in the absorber, and hence the QE is lower.[86]

3.3. Comparison of SCAPS-1D Results with Previous Work. Table 5 shows a comparison of our results with the current theoretical and experimental research on lead-free $CsSnI_3$-based PSCs with different configurations. Here, we have disclosed the maximum PCE of 10.1%, while previous studies like experimental and simulation reached up to 3.83 and 6.40%, respectively. Additionally, we performed a thorough simulation to identify an efficient ETL, HTL, and its various characteristics. However, the goal of all of these simulations was to find the perfect combinations that would produce the best results. Except this, in comparison with all the previous simulation results, all the six studied devices' performance was significant, which may help to identify more effective configurations for the near future.

4. CONCLUSIONS

The ideal direct band gap, low exciton binding energy, high absorption coefficient, and superior carrier mobility are some of the attractive features, which have established $CsSnI_3$ as a

https://doi.org/10.1021/acsomega.3c00306
ACS Omega 2023, 8, 22466−22485

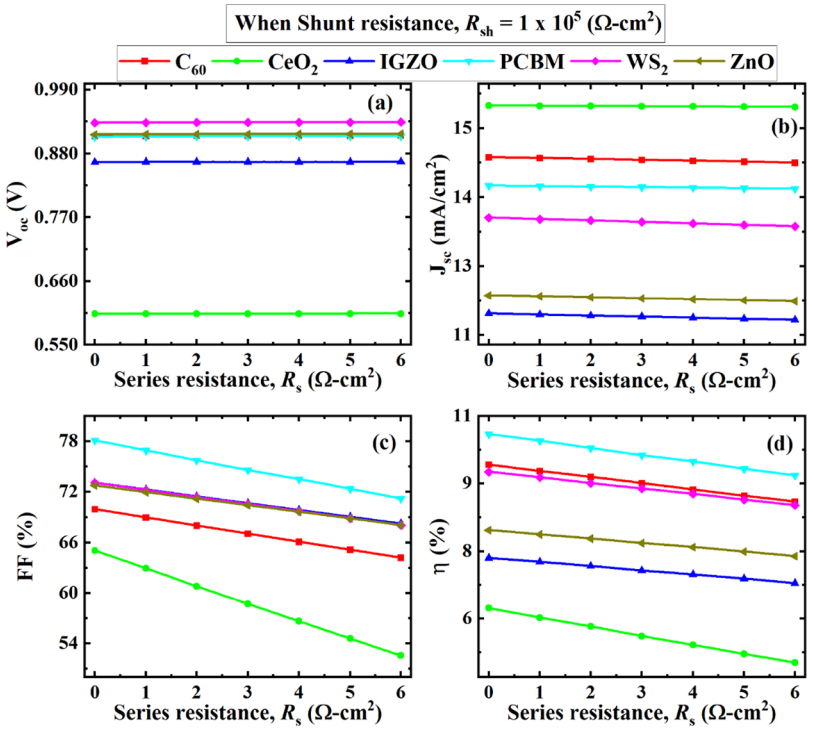

Figure 10. Effect of change of R_S on PV parameters (a) V_{OC}, (b) J_{SC}, (c) FF, and (d) PCE with a constant R_{SH} for different ETLs.

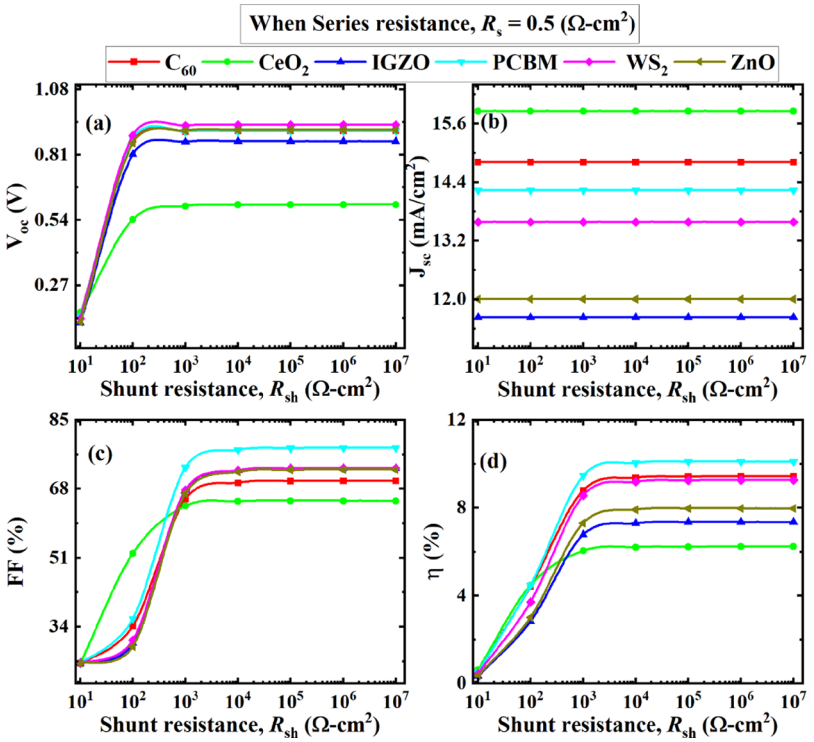

Figure 11. Effect of change of R_{SH} on PV parameters (a) V_{OC}, (b) J_{SC}, (c) FF, and (d) PCE with constant R_S for different ETLs.

dominant absorber material for lead-free PV applications. In the present study, we performed first-principle computations using the CASTEP program to examine the structural geometry and electronic and optical properties of the $CsSnI_3$ ($Pm\bar{3}m$ symmetry). Additionally, 70 different configurations of PSC using the $CsSnI_3$ absorber are numerically tested using SCAPS-1D simulations in terms of PV performance, out of which six optimized best-performing PSCs are chosen for a detailed analysis. The main highlights of this exhaustive research work are summarized below:

(1) From the DFT calculations, we found that $CsSnI_3$ exhibits a band gap of 0.95 eV, isotropic charge distribution in every crystalline plane, and multiband character with both electron-like and hole-like Fermi surfaces. It also possesses a high absorption coefficient, lower reflectivity

https://doi.org/10.1021/acsomega.3c00306
ACS Omega 2023, 8, 22466−22485

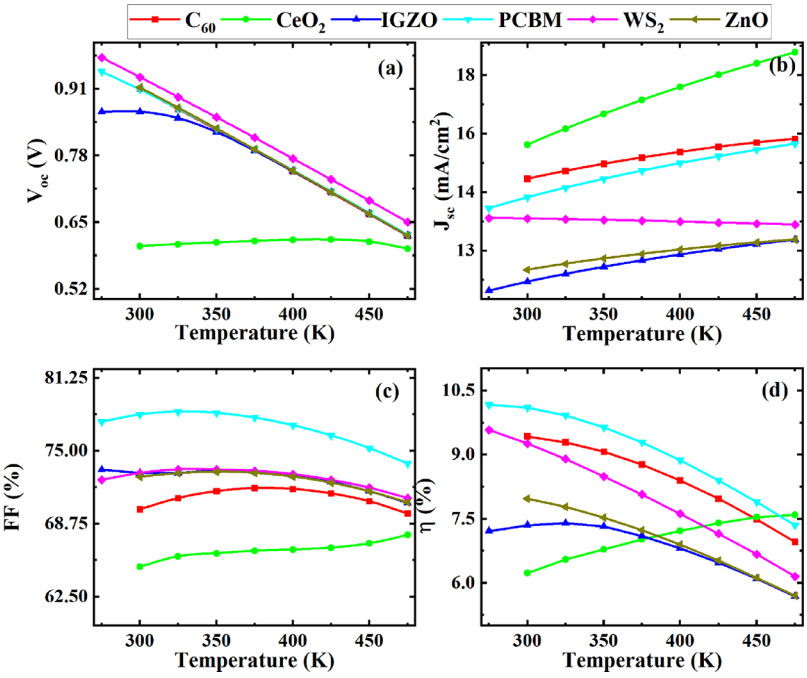

Figure 12. Effect of change of temperature on PV parameters (a) V_{OC}, (b) J_{SC}, (c) FF, and (d) PCE for different ETLs.

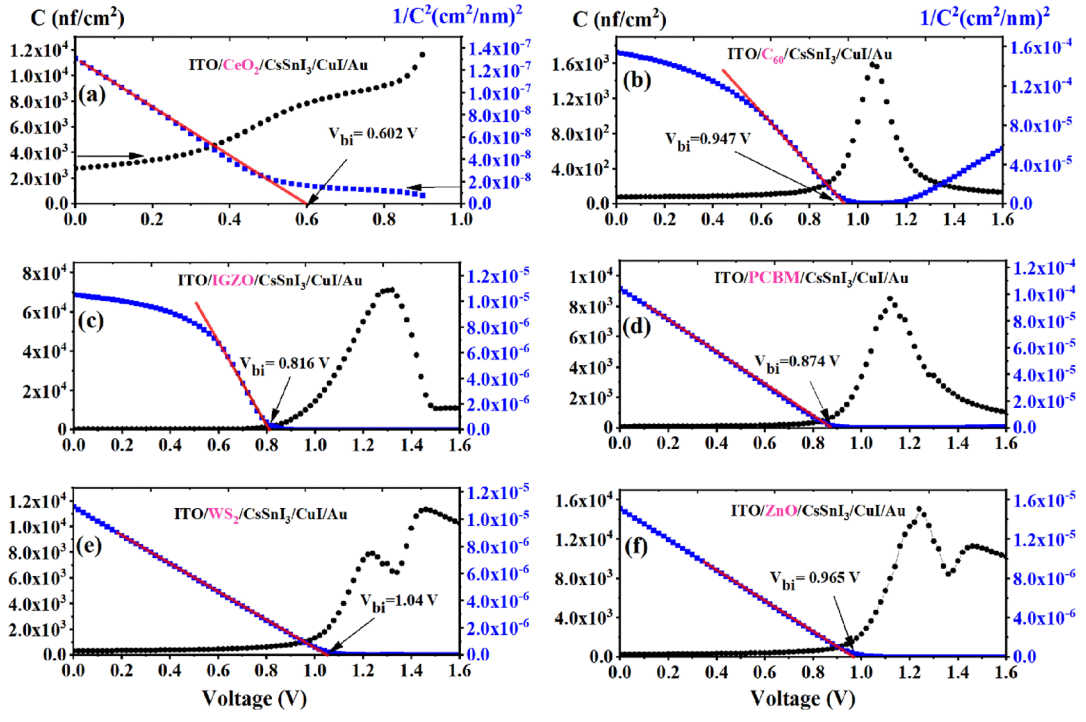

Figure 13. (a) Capacitance and Mott−Schottky ($1/C^2$) plot for the $CsSnI_3$-based perovskite solar cell having different ETLs (a) CeO_2 (b) C_{60}, (c) IGZO, (d) PCBM, (e) WS_2, and (f) ZnO.

than $CsSnCl_3$, and high conductivity that can be used for potential optoelectronic applications in UV and visible range.

(2) For the ITO/ETL/$CsSnI_3$/HTL/Au heterostructures, it is found that PSCs with ETLs such as PCBM, C_{60}, and WS_2 resulted in higher efficiencies in the range of 9−10%, while other ETLs like ZnO, IGZO, TiO_2, and CeO_2 exhibited lower efficiencies of ≤8%. The PV performance is controlled significantly by the band alignment between the ETL, HTL, and the perovskite $CsSnI_3$. CuI also acts as the best HTL out of the investigated HTLs due to its high band gap and superior absorption coefficient.

(3) The effect of the simultaneous variation of the absorber layer and ETL thickness on PV parameters revealed that with the rise in the thickness of these layers, the PV performance starts to degrade significantly.

(4) It is evident from the analysis of different SC structures that ITO/PCBM/$CsSnI_3$/CuI/Au displays the highest

https://doi.org/10.1021/acsomega.3c00306
ACS Omega 2023, 8, 22466−22485

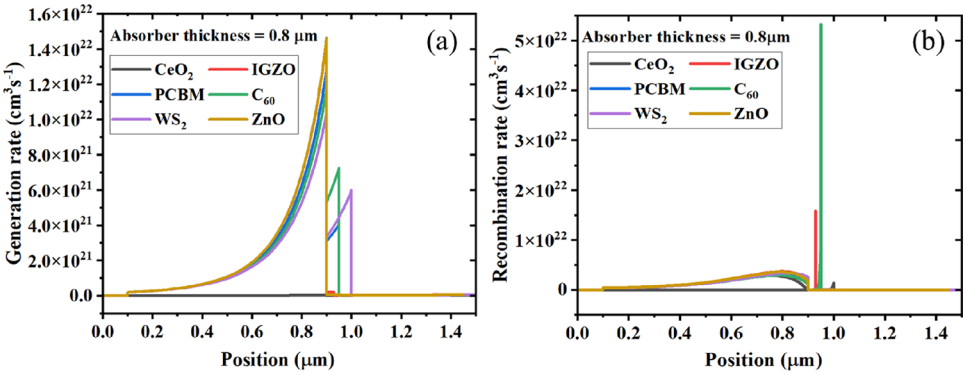

Figure 14. (a) Generation rate and (b) recombination rate for absorber $CsSnI_3$-based structures with six different ETLs.

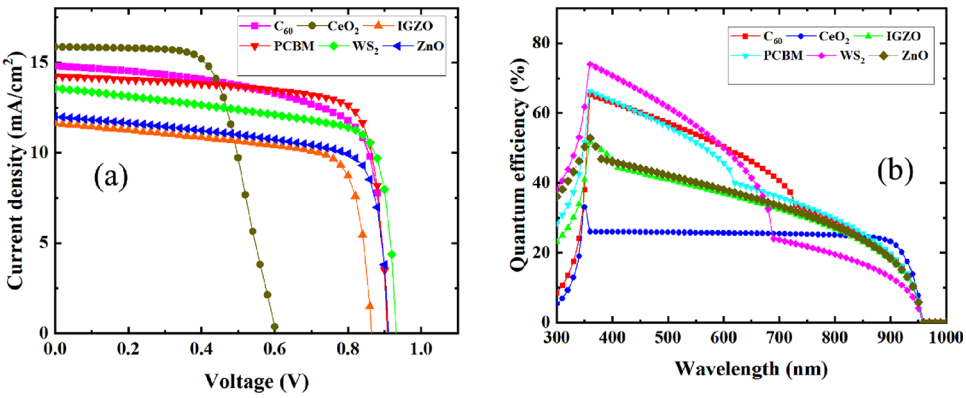

Figure 15. (a) $J-V$ curve for six studied structures of ITO/ETL/$CsSnI_3$/CuI/Au; (b) QE curve for the structure of ITO/ETL/$CsSnI_3$/CuI/Au.

Table 5. Comparison of PV Parameters of $CsSnI_3$-Based Solar Cells[b]

type	device structure	V_{oc} (V)	J_{sc} (mA/cm^2)	FF (%)	PCE (%)	ref
1	FTO/TiO_2/$CsSnI_3$/Au	0.34	20.63	54.18	3.83	87
1	FTO/TiO_2/$CsSnI_3$/m-MTDATA/Au	0.24	22.70	0.37	2.02	24
2	ITO/TiO_2/$MASnI_3$/Spiro-OMeTAD/Au	0.88	16.80	0.42	6.40	88
2	ITO/PCBM/$CsSnI_3$/NiO_2/Al	0.52	10.21	62.50	3.31	89
2	ITO/PCBM/$CsSnI_3$/CuI/Au	0.91	14.24	78.11	10.10	[a]
2	ITO/ZnO/$CsSnI_3$/CuI/Au	0.91	12.01	72.76	7.97	[a]
2	ITO/C_{60}/$CsSnI_3$/CuI/Au	0.91	14.81	69.99	9.43	[a]
2	ITO/IGZO/$CsSnI_3$/CuI/Au	0.87	11.63	73.09	7.35	[a]
2	ITO/WS_2/CsSnI3/CuI/Au	0.93	13.59	73.08	9.26	[a]
2	ITO/CeO_2/$CsSnI_3$/CuI/Au	0.60	15.86	65.06	6.23	[a]

[a]This work. [b]1: Experimental; 2: theoretical.

performance with a PCE of 10.10%, an FF of 78.11%, a J_{SC} of 14.24 mA/cm^2, and a V_{OC} of 0.91 V.

The results obtained using the best configurations are further validated through an extensive analysis of the effect of series and shunt resistance and the operating temperature on the PV parameters. Capacitance, Mott–Schottky, generation and recombination rates, $J-V$, and QE characteristics of these structures are analyzed for a deep-level understanding of mechanisms guiding the PV performance. This methodical study can open fruitful pathways for the fabrication of low-cost, high-efficiency, and lead-free $CsSnI_3$ perovskite-based high-performance SCs for a lead-free natural environment.

■ ASSOCIATED CONTENT

Data Availability Statement

The raw/processed data required to reproduce these findings cannot be shared at this time as the data also forms part of an ongoing study.

■ AUTHOR INFORMATION

Corresponding Authors

M. Khalid Hossain − *Institute of Electronics, Atomic Energy Research Establishment, Bangladesh Atomic Energy Commission, Dhaka 1349, Bangladesh; Department of Advanced Energy Engineering Science, Interdisciplinary Graduate School of Engineering Sciences, Kyushu University, Fukuoka 816-8580, Japan;* orcid.org/0000-0003-4595-6367; Email: khalid.baec@gmail.com, khalid@kyudai.jp

D. P. Samajdar − *Department of ECE, Indian Institute of Information Technology, Design & Manufacturing, Jabalpur 482005 Madhya Pradesh, India;* orcid.org/0000-0001-9518-2692; Email: dipprakash010@gmail.com

M. H. K. Rubel − *Department of Materials Science and Engineering, University of Rajshahi, Rajshahi 6205, Bangladesh;* orcid.org/0000-0001-9420-4335; Email: mhk_mse@ru.ac.bd

Rahul Pandey − *VLSI Centre of Excellence, Chitkara University Institute of Engineering and Technology, Chitkara University,*

https://doi.org/10.1021/acsomega.3c00306
ACS Omega 2023, 8, 22466−22485

Punjab 140401, India; orcid.org/0000-0001-7766-3572; Email: rahul.pandey@chitkara.edu.in

Authors

G. F. Ishraque Toki − *College of Materials Science and Engineering, Donghua University, Shanghai 201620, China*

Muhammad Mushtaq − *Department of Physics, University of Poonch Rawalakot, Rawalakot 12350, Pakistan;* orcid.org/0000-0001-5496-2836

Jaya Madan − *VLSI Centre of Excellence, Chitkara University Institute of Engineering and Technology, Chitkara University, Punjab 140401, India*

Mustafa K. A. Mohammed − *Radiological Techniques Department, Al-Mustaqbal University College, 51001 Hillah, Babylon, Iraq;* orcid.org/0000-0002-1850-6355

Md. Rasidul Islam − *Department of Electrical and Electronic Engineering, Bangamata Sheikh Fojilatunnesa Mujib Science & Technology University, Jamalpur 2012, Bangladesh*

Md. Ferdous Rahman − *Department of Electrical and Electronic Engineering, Begum Rokeya University, Rangpur 5400, Bangladesh*

H. Bencherif − *LEREESI, Higher National School of Renewable Energies, Environment and Sustainable Development, Batna 05078, Algeria*

Complete contact information is available at: https://pubs.acs.org/10.1021/acsomega.3c00306

Funding

This research did not receive any specific grant from funding agencies in the public, commercial, or not-for-profit sectors.

Notes

The authors declare no competing financial interest.

■ ACKNOWLEDGMENTS

The SCAPS-1D program was kindly provided by Dr. M. Burgelman of the University of Gent in Belgium. The authors would like to express their gratitude to him.

■ REFERENCES

(1) Ye, T.; Wang, K.; Hou, Y.; Yang, D.; Smith, N.; Magill, B.; Yoon, J.; Mudiyanselage, R. R. H. H.; Khodaparast, G. A.; Wang, K.; Priya, S. Ambient-Air-Stable Lead-Free $CsSnI_3$ Solar Cells with Greater than 7.5% Efficiency. *J. Am. Chem. Soc.* **2021**, *143*, 4319−4328.

(2) Stranks, S. D.; Snaith, H. J. Metal-Halide Perovskites for Photovoltaic and Light-Emitting Devices. *Nat. Nanotechnol.* **2015**, *10*, 391−402.

(3) Zhou, Y.; Zhu, K. Perovskite Solar Cells Shine in the "Valley of the Sun". *ACS Energy Lett.* **2016**, *1*, 64−67.

(4) Yang, M.; Zhou, Y.; Zeng, Y.; Jiang, C.-S.; Padture, N. P.; Zhu, K. Square-Centimeter Solution-Processed Planar $CH_3NH_3PbI_3$ Perovskite Solar Cells with Efficiency Exceeding 15%. *Adv. Mater.* **2015**, *27*, 6363−6370.

(5) Zhou, Y.; Yang, M.; Pang, S.; Zhu, K.; Padture, N. P. Exceptional Morphology-Preserving Evolution of Formamidinium Lead Triiodide Perovskite Thin Films via Organic-Cation Displacement. *J. Am. Chem. Soc.* **2016**, *138*, 5535−5538.

(6) Islam, M. R.; Mazumder, A. A. M.; Mojumder, M. R. H.; Shifat, A. S. M. Z.; Hossain, M. K. Strain-Induced Tunable Optoelectronic Properties of Inorganic Halide Perovskites $APbCl_3$ (A = K, Rb, and Cs). *Jpn. J. Appl. Phys.* **2023**, *62*, No. 011002.

(7) Thakur, A.; Singh, D.; Kaur Gill, S. Numerical Simulations of 26.11% Efficient Planar CH3NH3PbI3 Perovskite n-i-p Solar Cell. *Mater. Today: Proc.* **2022**, *71*, 195−201.

(8) Dureja, T.; Garg, A.; Bhalla, S.; Bhutani, D.; Khanna, A. Double Lead-Free Perovskite Solar Cell for 19.9% Conversion Efficiency: A SCAPS-1D Based Simulation Study. *Mater. Today: Proc.* **2022**, *71*, 239−242.

(9) Bencherif, H.; Meddour, F.; Elshorbagy, M. H.; Hossain, M. K.; Cuadrado, A.; Abdi, M. A.; Bendib, T.; Kouda, S.; Alda, J. Performance Enhancement of $(FAPbI_3)_{1-x}(MAPbBr_3)_x$ Perovskite Solar Cell with an Optimized Design. *Micro Nanostruct.* **2022**, *171*, No. 207403.

(10) Bencherif, H.; Hossain, M. K. Design and Numerical Investigation of Efficient $(FAPbI_3)_{1-x}(CsSnI_3)_x$ Perovskite Solar Cell with Optimized Performances. *Sol. Energy* **2022**, *248*, 137−148.

(11) Lotsch, B. V. New Light on an Old Story: Perovskites Go Solar. *Angew. Chem., Int. Ed.* **2014**, *53*, 635−637.

(12) Abate, A. Perovskite Solar Cells Go Lead Free. *Joule* **2017**, *1*, 659−664.

(13) Zhao, S.; Cai, W.; Wang, H.; Zang, Z.; Chen, J. All-Inorganic Lead-Free Perovskite(-Like) Single Crystals: Synthesis, Properties, and Applications. *Small Methods* **2021**, *5*, 2001308.

(14) Conings, B.; Drijkoningen, J.; Gauquelin, N.; Babayigit, A.; D'Haen, J.; D'Olieslaeger, L.; Ethirajan, A.; Verbeeck, J.; Manca, J.; Mosconi, E.; De Angelis, F.; Boyen, H.-G. Intrinsic Thermal Instability of Methylammonium Lead Trihalide Perovskite. *Adv. Energy Mater.* **2015**, *5*, 1500477.

(15) Zhang, Y.-Y.; Chen, S.; Xu, P.; Xiang, H.; Gong, X.-G.; Walsh, A.; Wei, S.-H. Intrinsic Instability of the Hybrid Halide Perovskite Semiconductor $CH_3NH_3PbI_3$. *Chin. Phys. Lett.* **2018**, *35*, No. 036104.

(16) Eperon, G. E.; Paternò, G. M.; Sutton, R. J.; Zampetti, A.; Haghighirad, A. A.; Cacialli, F.; Snaith, H. J. Inorganic Caesium Lead Iodide Perovskite Solar Cells. *J. Mater. Chem. A* **2015**, *3*, 19688−19695.

(17) Beal, R. E.; Slotcavage, D. J.; Leijtens, T.; Bowring, A. R.; Belisle, R. A.; Nguyen, W. H.; Burkhard, G. F.; Hoke, E. T.; McGehee, M. D. Cesium Lead Halide Perovskites with Improved Stability for Tandem Solar Cells. *J. Phys. Chem. Lett.* **2016**, *7*, 746−751.

(18) Chung, I.; Song, J.-H.; Im, J.; Androulakis, J.; Malliakas, C. D.; Li, H.; Freeman, A. J.; Kenney, J. T.; Kanatzidis, M. G. $CsSnI_3$: Semiconductor or Metal? High Electrical Conductivity and Strong Near-Infrared Photoluminescence from a Single Material. High Hole Mobility and Phase-Transitions. *J. Am. Chem. Soc.* **2012**, *134*, 8579−8587.

(19) Zhou, Y.; Garces, H. F.; Senturk, B. S.; Ortiz, A. L.; Padture, N. P. Room Temperature "One-Pot" Solution Synthesis of Nanoscale $CsSnI_3$ Orthorhombic Perovskite Thin Films and Particles. *Mater. Lett.* **2013**, *110*, 127−129.

(20) Dang, Y.; Zhou, Y.; Liu, X.; Ju, D.; Xia, S.; Xia, H.; Tao, X. Formation of Hybrid Perovskite Tin Iodide Single Crystals by Top-Seeded Solution Growth. *Angew. Chem., Int. Ed.* **2016**, *55*, 3447−3450.

(21) Chung, I.; Lee, B.; He, J.; Chang, R. P. H.; Kanatzidis, M. G. All-Solid-State Dye-Sensitized Solar Cells with High Efficiency. *Nature* **2012**, *485*, 486−489.

(22) Chen, Z.; Yu, C.; Shum, K.; Wang, J. J.; Pfenninger, W.; Vockic, N.; Midgley, J.; Kenney, J. T. Photoluminescence Study of Polycrystalline $CsSnI_3$ Thin Films: Determination of Exciton Binding Energy. *J. Lumin.* **2012**, *132*, 345−349.

(23) Shum, K.; Chen, Z.; Qureshi, J.; Yu, C.; Wang, J. J.; Pfenninger, W.; Vockic, N.; Midgley, J.; Kenney, J. T. Synthesis and Characterization of $CsSnI_3$ Thin Films. *Appl. Phys. Lett.* **2010**, *96*, No. 221903.

(24) Kumar, M. H.; Dharani, S.; Leong, W. L.; Boix, P. P.; Prabhakar, R. R.; Baikie, T.; Shi, C.; Ding, H.; Ramesh, R.; Asta, M.; Graetzel, M.; Mhaisalkar, S. G.; Mathews, N. Lead-Free Halide Perovskite Solar Cells with High Photocurrents Realized Through Vacancy Modulation. *Adv. Mater.* **2014**, *26*, 7122−7127.

(25) Chen, Z.; Wang, J. J.; Ren, Y.; Yu, C.; Shum, K. Schottky Solar Cells Based on $CsSnI_3$ Thin-Films. *Appl. Phys. Lett.* **2012**, *101*, No. 093901.

(26) Shrivastav, N.; Kashyap, S.; Madan, J.; Al-Mousoi, A. K.; Mohammed, M. K. A.; Hossain, M. K.; Pandey, R.; Ramanujam, J. Perovskite-CIGS Monolithic Tandem Solar Cells with 29.7% Efficiency: A Numerical Study. *Energy Fuels* **2023**, *37*, 3083−3090.

(27) Kashyap, S.; Madan, J.; Mohammed, M. K. A.; Hossain, M. K.; Ponnusamy, S.; Pandey, R. Unlocking the Potential of MgF_2 Textured

Surface in Enhancing the Efficiency of Perovskite Solar Cells. *Mater. Lett.* **2023**, *339*, No. 134096.
(28) Pandey, R.; Bhattarai, S.; Sharma, K.; Madan, J.; Al-Mousoi, A. K.; Mohammed, M. K. A.; Hossain, M. K. Halide Composition Engineered a Non-Toxic Perovskite−Silicon Tandem Solar Cell with 30.7% Conversion Efficiency. *ACS Appl. Electron. Mater.* 2023, DOI: 10.1021/acsaelm.2c01574.
(29) Hossain, M. K.; Toki, G. F. I.; Alam, I.; Pandey, R.; Samajdar, D. P.; Rahman, M. F.; Islam, M. R.; Rubel, M. H. K.; Bencherif, H.; Madan, J.; Mohammed, M. K. A. Numerical Simulation and Optimization of a CsPbI 3 -Based Perovskite Solar Cell to Enhance the Power Conversion Efficiency. *New J. Chem.* **2023**, *47*, 4801−4817.
(30) Chiang, Y.-F.; Jeng, J.-Y.; Lee, M.-H.; Peng, S.-R.; Chen, P.; Guo, T.-F.; Wen, T.-C.; Hsu, Y.-J.; Hsu, C.-M. High Voltage and Efficient Bilayer Heterojunction Solar Cells Based on an Organic−Inorganic Hybrid Perovskite Absorber with a Low-Cost Flexible Substrate. *Phys. Chem. Chem. Phys.* **2014**, *16*, 6033−6040.
(31) Ryu, S.; Noh, J. H.; Jeon, N. J.; Chan Kim, Y.; Yang, W. S.; Seo, J.; Seok, S. I. Voltage Output of Efficient Perovskite Solar Cells with High Open-Circuit Voltage and Fill Factor. *Energy Environ. Sci.* **2014**, *7*, 2614−2618.
(32) Yusoff, A. R. b. M.; Nazeeruddin, M. K. Organohalide Lead Perovskites for Photovoltaic Applications. *J. Phys. Chem. Lett.* **2016**, *7*, 851−866.
(33) Raoui, Y.; Ez-Zahraouy, H.; Tahiri, N.; El Bounagui, O.; Ahmad, S.; Kazim, S. Performance Analysis of $MAPbI_3$ Based Perovskite Solar Cells Employing Diverse Charge Selective Contacts: Simulation Study. *Sol. Energy* **2019**, *193*, 948−955.
(34) Abdelaziz, S.; Zekry, A.; Shaker, A.; Abouelatta, M. Investigating the Performance of Formamidinium Tin-Based Perovskite Solar Cell by SCAPS Device Simulation. *Opt. Mater.* **2020**, *101*, No. 109738.
(35) Basher, M. K.; Shah Riyadh, S. M.; Hossain, M. K.; Hassan, M.; Akand, M. A. R.; Amir-Al Zumahi, S. M.; Matin, M. A.; Das, N.; Nur-E-Alam, M. Development of Zinc-Oxide Nanorods on Chemically Etched Zinc Plates Suitable for High-Efficiency Photovoltaics Solar Cells. *Opt. Quant. Electron.* **2023**, *55*, 322.
(36) Gan, Y.; Bi, X.; Liu, Y.; Qin, B.; Li, Q.; Jiang, Q.; Mo, P. Numerical Investigation Energy Conversion Performance of Tin-Based Perovskite Solar Cells Using Cell Capacitance Simulator. *Energies* **2020**, *13*, 5907.
(37) Hossain, M. K.; Toki, G. F. I.; Kuddus, A.; Rubel, M. H. K.; Hossain, M. M.; Bencherif, H.; Rahman, M. F.; Islam, M. R.; Mushtaq, M. An Extensive Study on Multiple ETL and HTL Layers to Design and Simulation of High-Performance Lead-Free $CsSnCl_3$-Based Perovskite Solar Cells. *Sci. Rep.* **2023**, *13*, 2521.
(38) Sobayel, K.; Akhtaruzzaman, M.; Rahman, K. S.; Ferdaous, M. T.; Al-Mutairi, Z. A.; Alharbi, H. F.; Alharthi, N. H.; Karim, M. R.; Hasmady, S.; Amin, N. A Comprehensive Defect Study of Tungsten Disulfide (WS_2) as Electron Transport Layer in Perovskite Solar Cells by Numerical Simulation. *Results Phys.* **2019**, *12*, 1097−1103.
(39) Hossain, M. K.; Arnab, A. A.; Das, R. C.; Hossain, K. M.; Rubel, M. H. K.; Rahman, M. F.; Bencherif, H.; Emetere, M. E.; Mohammed, M. K. A.; Pandey, R. Combined DFT, SCAPS-1D, and WxAMPS Frameworks for Design Optimization of Efficient Cs_2BiAgI_6-Based Perovskite Solar Cells with Different Charge Transport Layers. *RSC Adv.* **2022**, *12*, 34850−34873.
(40) Khatun, M. M.; Sunny, A.; Al A hmed, S. R. Numerical Investigation on Performance Improvement of WS_2 Thin-Film Solar Cell with Copper Iodide as Hole Transport Layer. *Sol. Energy* **2021**, *224*, 956−965.
(41) Khattak, Y. H.; Baig, F.; Toura, H.; Beg, S.; Soucase, B. M. CZTSe Kesterite as an Alternative Hole Transport Layer for $MASnI_3$ Perovskite Solar Cells. *J. Electron. Mater.* **2019**, *48*, 5723−5733.
(42) Islam, M. R.; Islam, M. S.; Zamil, M. Y.; Ferdous, N.; Stampfl, C.; Park, J.; Hossain, M. K. Two-Dimensional BAs/GeC van Der Waals Heterostructures: A Widely Tunable Photocatalyst for Water Splitting and Hydrogen Production. *J. Phys. Chem. Solids* **2023**, *176*, No. 111263.
(43) van Mourik, T.; Bühl, M.; Gaigeot, M.-P. Density Functional Theory across Chemistry, Physics and Biology. *Philos. Trans. R. Soc., A* **2014**, *372*, 20120488.
(44) Song, G.; Gao, B.; Li, G.; Zhang, J. First-Principles Study on the Electric Structure and Ferroelectricity in Epitaxial $CsSnI_3$ Films. *RSC Adv.* **2017**, *7*, 41077−41083.
(45) Huang, L.; Lambrecht, W. R. L. Electronic Band Structure, Phonons, and Exciton Binding Energies of Halide Perovskites $CsSnCl_3$, $CsSnBr_3$, and $CsSnI_3$. *Phys. Rev. B* **2013**, *88*, No. 165203.
(46) Yu, C.; Chen, Z.; Wang, J.; Pfenninger, W.; Vockic, N.; Kenney, J. T.; Shum, K. Temperature Dependence of the Band Gap of Perovskite Semiconductor Compound $CsSnI_3$. *J. Appl. Phys.* **2011**, *110*, No. 063526.
(47) Traoré, B.; Bouder, G.; Lafargue-Dit-Hauret, W.; Rocquefelte, X.; Katan, C.; Tran, F.; Kepenekian, M. Efficient and Accurate Calculation of Band Gaps of Halide Perovskites with the Tran-Blaha Modified Becke-Johnson Potential. *Phys. Rev. B* **2019**, *99*, No. 035139.
(48) Clark, S. J.; Segall, M. D.; Pickard, C. J.; Hasnip, P. J.; Probert, M. I. J.; Refson, K.; Payne, M. C. First Principles Methods Using CASTEP. *Z. fur Krist. - Cryst. Mater* **2005**, *220*, 567−570.
(49) Perdew, J. P.; Ruzsinszky, A.; Csonka, G. I.; Vydrov, O. A.; Scuseria, G. E.; Constantin, L. A.; Zhou, X.; Burke, K. Restoring the Density-Gradient Expansion for Exchange in Solids and Surfaces. *Phys. Rev. Lett.* **2008**, *100*, No. 136406.
(50) Vanderbilt, D. Soft Self-Consistent Pseudopotentials in a Generalized Eigenvalue Formalism. *Phys. Rev. B* **1990**, *41*, 7892−7895.
(51) Rahman, M. F.; Alam Moon, M. M.; Hossain, M. K.; Ali, M. H.; Haque, M. D.; Kuddus, A.; Hossain, J.; Md. Ismail, A. B. Concurrent Investigation of Antimony Chalcogenide (Sb_2Se_3 and Sb_2S_3)-Based Solar Cells with a Potential WS_2 Electron Transport Layer. *Heliyon* **2022**, *8*, No. e12034.
(52) Hasan Ali, M.; Saiful Islam, A. T. M.; Haque, M. D.; Ferdous Rahman, M.; Khalid Hossain, M.; Sultana, N.; Touhidul Islam, A. Z. M. Numerical Analysis of $FeSi_2$ Based Solar Cell with PEDOT:PSS Hole Transport Layer. *Mater. Today Commun.* **2023**, *34*, No. 105387.
(53) Rahman, M. F.; Habib, M. J. A.; Ali, M. H.; Rubel, M. H. K.; Islam, M. R.; Ismail, A. B. M.; Hossain, M. K. Design and Numerical Investigation of Cadmium Telluride (CdTe) and Iron Silicide ($FeSi_2$) Based Double Absorber Solar Cells to Enhance Power Conversion Efficiency. *AIP Adv.* **2022**, *12*, 105317.
(54) Ali, M. H.; Al Mamun, M. A.; Haque, M. D.; Rahman, M. F.; Hossain, M. K.; Md. Touhidul Islam, A. Z. Performance Enhancement of an MoS_2-Based Heterojunction Solar Cell with an In_2Te_3 Back Surface Field: A Numerical Simulation Approach. *ACS Omega* **2023**, *8*, 7017−7029.
(55) Mohammed, M. K. A.; Al-Mousoi, A. K.; Singh, S.; Kumar, A.; Hossain, M. K.; Salih, S. Q.; Sasikumar, P.; Pandey, R.; Yadav, A. A.; Yaseen, Z. M. Improving the Performance of Perovskite Solar Cells with Carbon Nanotubes as a Hole Transport Layer. *Opt. Mater.* **2023**, *138*, No. 113702.
(56) Rahman, M. F.; Mahmud, N.; Alam, I.; Ali, M. H.; Moon, M. M. A.; Kuddus, A.; Toki, G. F. I.; Rubel, M. H. K.; Asad, M. A.; Al Hossain, M. K. Design and Numerical Analysis of CIGS-Based Solar Cell with V_2O_5 as the BSF Layer to Enhance Photovoltaic Performance. *AIP Adv.* **2023**, *13*, No. 045309.
(57) Jabr, R. A.; Hamad, M.; Mohanna, Y. M. Newton-Raphson Solution of Poisson's Equation in a Pn Diode. *Int. J. Electr. Eng. Educ.* **2007**, *44*, 23−33.
(58) Hossain, M. K.; Pervez, M. F.; Mia, M. N. H.; Mortuza, A. A.; Rahaman, M. S.; Karim, M. R.; Islam, J. M. M.; Ahmed, F.; Khan, M. A. Effect of Dye Extracting Solvents and Sensitization Time on Photovoltaic Performance of Natural Dye Sensitized Solar Cells. *Results Phys.* **2017**, *7*, 1516−1523.
(59) Lin, P.; Lin, L.; Yu, J.; Cheng, S.; Lu, P.; Zheng, Q. Numerical Simulation of Cu_2ZnSnS_4 Based Solar Cells with In_2S_3 Buffer Layers by SCAPS-1D. *J. Appl. Sci. Eng.* **2014**, *17*, 383−390.
(60) Hossain, M. K.; Rubel, M. H. K.; Toki, G. F. I.; Alam, I.; Rahman, M. F.; Bencherif, H. Effect of Various Electron and Hole Transport Layers on the Performance of $CsPbI_3$-Based Perovskite Solar Cells: A

Numerical Investigation in DFT, SCAPS-1D, and WxAMPS Frameworks. *ACS Omega* **2022**, *7*, 43210−43230.
(61) Srivastava, S.; Singh, A. K.; Kumar, P.; Pradhan, B. Comparative Performance Analysis of Lead-Free Perovskites Solar Cells by Numerical Simulation. *J. Appl. Phys.* **2022**, *131*, 175001.
(62) Xu, X.; Wang, J.; Cao, D.; Zhou, Y.; Jiao, Z. Design of All-Inorganic Hole-Transport-Material-Free $CsPbI_3/CsSnI_3$ heterojunction Solar Cells by Device Simulation. *Mater. Res. Express* **2022**, *9*, No. 025509.
(63) Zhou, Y.; Zhao, Y. Chemical Stability and Instability of Inorganic Halide Perovskites. *Energy Environ. Sci.* **2019**, *12*, 1495−1511.
(64) Yamada, K.; Funabiki, S.; Horimoto, H.; Matsui, T.; Okuda, T.; Ichiba, S. Structural Phase Transitions of the Polymorphs of $CsSnI_3$ by Means of Rietveld Analysis of the X-Ray Diffraction. *Chem. Lett.* **1991**, *20*, 801−804.
(65) Nematov, D. D.; Burhonzoda, A. S.; Khusenov, M. A.; Kholmurodov, K. T.; Yamamoto, T. First Principles Analysis of Crystal Structure, Electronic and Optical Properties of $CsSnI_{3-x}Br_x$ Perovskite for Photoelectric Applications. *J. Surf. Invest.: X-Ray, Synchrotron Neutron Tech.* **2021**, *15*, 532−536.
(66) Rubel, M. H. K.; Mitro, S. K.; Hossain, M. K.; Hossain, K. M.; Rahaman, M. M.; Hossain, J.; Mondal, B. K.; Akter, A.; Rahman, M. F.; Ahmed, I.; Islam, A. K. M. A. First-Principles Calculations to Investigate Physical Properties of Single-Cubic $(Ba_{0.82}K_{0.18})(Bi_{0.53}Pb_{0.47})O_3$ Novel Perovskite Superconductor. *Mater. Today Commun.* **2022**, *33*, No. 104302.
(67) Rubel, M. H. K.; Hadi, M. A.; Rahaman, M. M.; Ali, M. S.; Aftabuzzaman, M.; Parvin, R.; Islam, A. K. M. A.; Kumada, N. Density Functional Theory Study of a New Bi-Based $(K_{1.00})$-$(Ba_{1.00})_3(Bi_{0.89}Na_{0.11})_4O_{12}$ Double Perovskite Superconductor. *Comput. Mater. Sci.* **2017**, *138*, 160−165.
(68) Karim, A. M. M. T.; Helal, M. A.; Alam, M. A.; Ali, M. A.; Ara, I.; Naqib, S. H. Optoelectronic, Thermodynamic and Vibrational Properties of Intermetallic $MgAl_2Ge_2$: A First-Principles Study. *SN Appl. Sci.* **2021**, *3*, 229.
(69) Rubel, M. H. K.; Hossain, M. A.; Hossain, M. K.; Hossain, K. M.; Khatun, A. A.; Rahaman, M. M.; Ferdous Rahman, M.; Hossain, M. M.; Hossain, J. First-Principles Calculations to Investigate Structural, Elastic, Electronic, Thermodynamic, and Thermoelectric Properties of $CaPd_3B_4O_{12}$ (B = Ti, V) Perovskites. *Results Phys.* **2022**, *42*, No. 105977.
(70) Hossain, M. M. First-Principles Study on the Structural, Elastic, Electronic and Optical Properties of $LiNbO_3$. *Heliyon* **2019**, *5*, No. e01436.
(71) Shiel, H.; Hutter, O. S.; Phillips, L. J.; Swallow, J. E. N.; Jones, L. A. H.; Featherstone, T. J.; Smiles, M. J.; Thakur, P. K.; Lee, T.-L.; Dhanak, V. R.; Major, J. D.; Veal, T. D. Natural Band Alignments and Band Offsets of Sb_2Se_3 Solar Cells. *ACS Appl. Energy Mater.* **2020**, *3*, 11617−11626.
(72) Minemoto, T.; Murata, M. Theoretical Analysis on Effect of Band Offsets in Perovskite Solar Cells. *Sol. Energy Mater. Sol. Cells* **2015**, *133*, 8−14.
(73) Cao, Y.; Zhu, X.; Chen, H.; Zhang, X.; Zhouc, J.; Hu, Z.; Pang, J. Towards High Efficiency Inverted Sb_2Se_3 Thin Film Solar Cells. *Sol. Energy Mater. Sol. Cells* **2019**, *200*, No. 109945.
(74) Xiao, Y.; Wang, H.; Kuang, H. Numerical Simulation and Performance Optimization of Sb_2S_3 Solar Cell with a Hole Transport Layer. *Opt. Mater. (Amst).* **2020**, *108*, No. 110414.
(75) Haider, S. Z.; Anwar, H.; Wang, M. A Comprehensive Device Modelling of Perovskite Solar Cell with Inorganic Copper Iodide as Hole Transport Material. *Semicond. Sci. Technol.* **2018**, *33*, No. 035001.
(76) Holzhey, P.; Saliba, M. A Full Overview of International Standards Assessing the Long-Term Stability of Perovskite Solar Cells. *J. Mater. Chem. A* **2018**, *6*, 21794−21808.
(77) Roesch, R.; Faber, T.; von Hauff, E.; Brown, T. M.; Lira-Cantu, M.; Hoppe, H. Procedures and Practices for Evaluating Thin-Film Solar Cell Stability. *Adv. Energy Mater.* **2015**, *5*, 1501407.
(78) Nakada, T.; Mizutani, M. 18% Efficiency Cd-Free Cu(In, Ga)Se_2 Thin-Film Solar Cells Fabricated Using Chemical Bath Deposition (CBD)-ZnS Buffer Layers. *Jpn. J. Appl. Phys.* **2002**, *41*, L165−L167.
(79) Khattak, Y. H.; Baig, F.; Ullah, S.; Marí, B.; Beg, S.; Ullah, H. Enhancement of the Conversion Efficiency of Thin Film Kesterite Solar Cell. *J. Renewable Sustainable Energy* **2018**, *10*, No. 033501.
(80) Samiul Islam, M.; Sobayel, K.; Al-Kahtani, A.; Islam, M. A.; Muhammad, G.; Amin, N.; Shahiduzzaman, M.; Akhtaruzzaman, M. Defect Study and Modelling of SnX_3-Based Perovskite Solar Cells with SCAPS-1D. *Nanomaterials* **2021**, *11*, 1218.
(81) Mamta; Maurya, K. K.; Singh, V. N. Sb_2Se_3/CZTS Dual Absorber Layer Based Solar Cell with 36.32% Efficiency: A Numerical Simulation. *J. Sci.: Adv. Mater. Devices* **2022**, *7*, No. 100445.
(82) Bisquert, J.; Garcia-Belmonte, G.; Munar, A.; Sessolo, M.; Soriano, A.; Bolink, H. J. Band Unpinning and Photovoltaic Model for P3HT:PCBM Organic Bulk Heterojunctions under Illumination. *Chem. Phys. Lett.* **2008**, *465*, 57−62.
(83) Qi, B.; Zhang, Z.-G.; Wang, J. Uncovering the Role of Cathode Buffer Layer in Organic Solar Cells. *Sci. Rep.* **2015**, *5*, 7803.
(84) Futscher, M. H.; Gangishetty, M. K.; Congreve, D. N.; Ehrler, B. Quantifying Mobile Ions and Electronic Defects in Perovskite-Based Devices with Temperature-Dependent Capacitance Measurements: Frequency vs Time Domain. *J. Chem. Phys.* **2020**, *152*, No. 044202.
(85) Almora, O.; Aranda, C.; Mas-Marzá, E.; Garcia-Belmonte, G. On Mott-Schottky Analysis Interpretation of Capacitance Measurements in Organometal Perovskite Solar Cells. *Appl. Phys. Lett.* **2016**, *109*, 173903.
(86) Lin, L.; Jiang, L.; Li, P.; Xiong, H.; Kang, Z.; Fan, B.; Qiu, Y. Simulated Development and Optimized Performance of $CsPbI_3$ Based All-Inorganic Perovskite Solar Cells. *Sol. Energy* **2020**, *198*, 454−460.
(87) Song, T.-B.; Yokoyama, T.; Logsdon, J.; Wasielewski, M. R.; Aramaki, S.; Kanatzidis, M. G. Piperazine Suppresses Self-Doping in $CsSnI_3$ Perovskite Solar Cells. *ACS Appl. Energy Mater.* **2018**, *1*, 4221−4226.
(88) Noel, N. K.; Stranks, S. D.; Abate, A.; Wehrenfennig, C.; Guarnera, S.; Haghighirad, A. A.; Sadhanala, A.; Eperon, G. E.; Pathak, S. K.; Johnston, M. B.; Petrozza, A.; Herz, L. M.; Snaith, H. J. Lead-Free Organic-Inorganic Tin Halide Perovskites for Photovoltaic Applications. *Energy Environ. Sci.* **2014**, *7*, 3061−3068.
(89) Wang, N.; Zhou, Y.; Ju, M.-G.; Garces, H. F.; Ding, T.; Pang, S.; Zeng, X. C.; Padture, N. P.; Sun, X. W. Heterojunction-Depleted Lead-Free Perovskite Solar Cells with Coarse-Grained B-γ-$CsSnI_3$ Thin Films. *Adv. Energy Mater.* **2016**, *6*, 1601130.

https://doi.org/10.1021/acsomega.3c00306
ACS Omega 2023, 8, 22466−22485